Surface radiative forcing by soil dust aerosols and the hydrologic cycle

R. L. Miller
Department of Applied Physics, Columbia University, New York, New York, USA

NASA Goddard Institute for Space Studies, New York, New York, USA

I. Tegen
Max Planck Institute for Biogeochemistry, Jena, Germany

Jan Perlwitz
Department of Applied Physics, Columbia University, New York, New York, USA

NASA Goddard Institute for Space Studies, New York, New York, USA

Received 18 August 2003; revised 5 December 2003; accepted 26 December 2003; published 21 February 2004.

[1] For absorbing aerosols like soil (or "mineral") dust, radiative forcing at the surface differs substantially from the value at the top of the atmosphere (TOA). The climate response depends not only upon the TOA forcing, but its difference with respect to the surface value, which represents radiative heating within the atmosphere. Surface forcing alters evaporation and the hydrologic cycle, which feeds back upon the aerosol burden through the efficiency of wet deposition. We calculate the surface forcing by soil dust aerosols and its global sensitivity by varying aspects of the dust distribution that are poorly constrained by observations. Ignorance of the global dust burden corresponds to a forcing uncertainty of over a factor of two, with smaller uncertainties due to imprecise knowledge of particle optical properties and the particle size distribution. While global evaporation and precipitation are reduced in response to surface radiative forcing by dust, precipitation increases locally over desert regions, so that dust emission can act as a negative feedback to desertification. The effect of the global reduction in precipitation is to lengthen the particle lifetime by reducing the efficiency of wet deposition, representing a positive feedback upon the global dust burden. For the current climate, we calculate the reduction in wet deposition by dust radiative forcing and find that the aerosol burden is increased only modestly. However, the global dust burden and associated radiative forcing are substantially higher during glacial climates, so that the amplification of the dust load by this feedback is larger. By extrapolating from its radiative forcing in the current climate, we estimate that dust reduces precipitation during glacial times by as much as half the reduction due to the colder climate alone. *INDEX TERMS:* 0305 Atmospheric Composition and Structure: Aerosols and particles (0345, 4801); 0360 Atmospheric Composition and Structure: Transmission and scattering of radiation; 1655 Global Change: Water cycles (1836); 3359 Meteorology and Atmospheric Dynamics: Radiative processes; *KEYWORDS:* dust aerosol, radiative forcing, hydrologic cycle

Citation: Miller, R. L., I. Tegen, and J. Perlwitz (2004), Surface radiative forcing by soil dust aerosols and the hydrologic cycle, *J. Geophys. Res.*, *109*, D04203, doi:10.1029/2003JD004085.

1. Introduction

[2] Soil (or "mineral") dust particles are the most common aerosol by mass [*Andreae*, 1995], entering the atmosphere through wind erosion of dry soils. While the atmospheric dust load is largest near deserts and soils disturbed by cultivation, the smallest particles, which are the most radiatively active by mass, can travel thousands of kilometers downwind of their source region. African dust is observed over both North and South America [*Prospero and Nees*, 1977; *Prospero et al.*, 1981; *Perry et al.*, 1997; *Prospero*, 1999], and to the east over the Indian Ocean [*Meywerk and Ramanathan*, 1999]. Soil dust from Asian deserts is measured at remote islands within the Pacific [*Duce et al.*, 1980; *Parrington et al.*, 1983; *Rea*, 1994], and as far downwind as North America and Greenland [*Biscaye et al.*, 1997; *Reader et al.*, 1999; *Bory et al.*, 2002; *Bory et al.*, 2003], and even Europe [*Grousset et al.*, 2003].

[3] The present-day distribution of dust must be inferred from a combination of data sources, as there is no single

0148-0227/04/2003JD004085$09.00

Table 1. Comparison of Global and Annual Average Dust Emission (Tg yr^{-1}), Load (Tg), Proportion of Clay to Silt Aerosol, and Lifetime (days) Between the Present Model and Recent Studies of Dust Transport

	Emission	Load	Proportion Clay: Silt	Lifetime		
				Wet	Dry	Total
Present model	1019	14.6	1: 0.59	12.8	8.9	5.2
Ginoux et al. [2001]	1814	35.9	1: 1.56	55.8	8.2	7.2
Tegen et al. [2002]	1100	22.2		21.7	11.2	7.4
Luo et al. [2003]	1654	23.3	1: 0.35	10.7	10.3	5.1
Zender et al. [2003a]	1490	17.4	1: 0.75	10.5	7.4	4.3

The models simulate particles with radii <10 μm. Clay particles are defined with radii <1 μm, except for the studies of *Luo et al.* [2003] and *Zender et al.* [2003a] where clay radii are as large as 1.25 μm.

definitive set of observations. Multidecadal surface measurements exist downwind of certain major source regions like the Sahara and Sahel [*Prospero*, 1996]. Column integrals of aerosols are provided by satellite retrievals [*Moulin et al.*, 1997; *Husar et al.*, 1997; *Herman et al.*, 1997; *King et al.*, 1999; *Torres et al.*, 2001] and sun photometers [*Holben et al.*, 1998], although the dust contribution is entangled with that of other aerosol species. The vertical distribution of dust within the column is revealed by LIDAR (Light Detection and Ranging) measurements, usually within detailed observing campaigns of limited duration [*Karyampudi et al.*, 1999]. Dust models are an effort to estimate the three dimensional distribution of dust and its evolution in time subject to all of these observational constraints [*Tegen and Fung*, 1994; *Guelle et al.*, 2000; *Ginoux et al.*, 2001; *Tegen et al.*, 2002; *Luo et al.*, 2003; *Zender et al.*, 2003a].

[4] While radiative forcing by soil dust has been recognized for decades [*Coakley and Cess*, 1985], its precise value remains unknown. The anthropogenic component, attributed to dry soils disturbed by agriculture, overgrazing, and deforestation, is possibly comparable to that of other tropospheric aerosols [*Tegen and Fung*, 1995; *Tegen et al.*, 1996; *Sokolik and Toon*, 1996; *Tegen et al.*, 1997; *Mahowald and Luo*, 2003], although this is still debated [*Haywood and Boucher*, 2000; *Ginoux et al.*, 2001; *Mahowald et al.*, 2002]. Unlike radiative forcing by greenhouse gases, which is fairly uniform throughout the troposphere [*Hansen et al.*, 1997a], forcing by dust and other tropospheric aerosols exhibit large regional variations due to their short lifetime. Downwind of major source regions, dust radiative forcing often dominates [*Li et al.*, 1996; *Chiapello et al.*, 1999].

[5] In contrast to sulfate aerosols formed by industrial pollution, dust particles absorb as well as scatter sunlight [*Lacis and Mishchenko*, 1995; *Tegen and Lacis*, 1996]. Absorption and scattering have offsetting effects upon solar forcing at the top of the atmosphere (TOA), while acting in concert to reduce forcing at the surface. Dust particles absorb at thermal wavelengths, contributing to positive forcing at both TOA and the surface. The effect of aerosols upon climate is often characterized by their forcing at TOA [*Intergovernmental Panel on Climate Change*, 2001]. However, for absorbing aerosols, the climate response depends not only upon the TOA forcing, but also upon its difference with respect to the surface value, which represents radiative heating within the atmosphere [*Miller and Tegen*, 1998; *Miller and Tegen*, 1999; *Ramanathan et al.*, 2001]. Indeed, the change in surface temperature in the former study is largely the result of this heating rather than the TOA forcing per se.

[6] This article calculates surface radiative forcing by soil dust aerosols, with emphasis upon its global uncertainty.

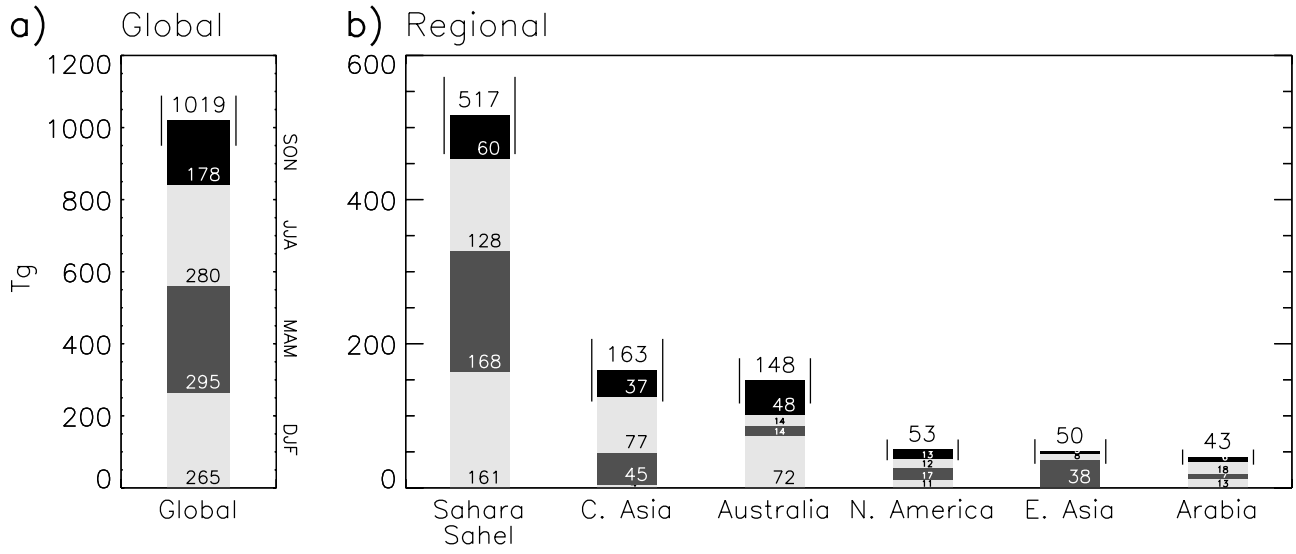

Figure 1. (a) Global and (b) regional emission of soil dust aerosol (Tg), as calculated by the AGCM. Each bar is divided into seasonal averages for DJF (bottom, light), MAM (above, dark), JJA, (above, light), and SON (top, dark). The annual average is given at the top of each bar. The vertical lines bracketing the annual average range between one standard deviation above and below. The Sahara/Sahel regional average is based upon Northern Hemisphere Africa gridboxes. Central Asia is defined between 25–90°E, 36–56°N; East Asia between 90–140°E, 32–52°N; and Arabia between 35–60°E but east of the Red Sea, and 12–36°N.

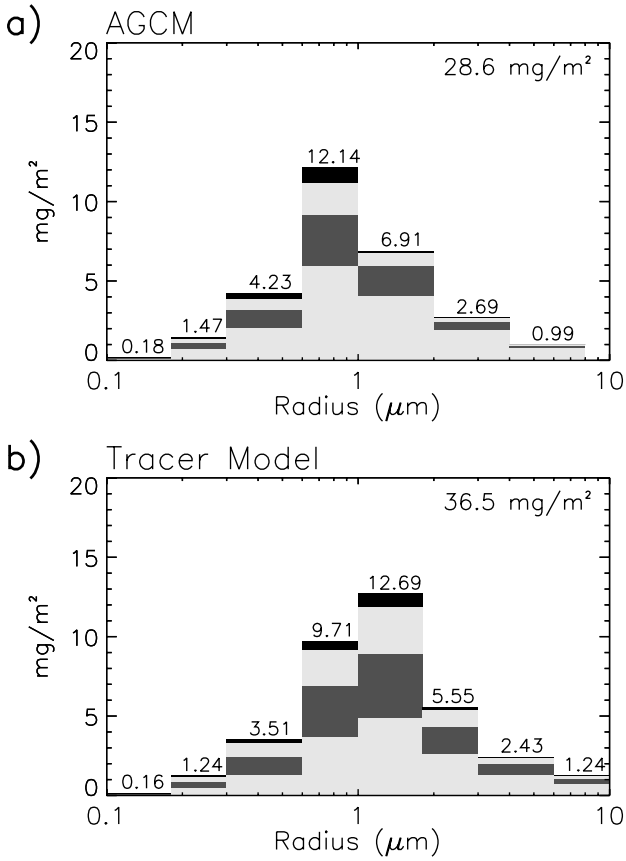

Figure 2. Contribution by each particle size category to the global and annual average dust load in mg m^{-2} as computed by (a) the AGCM, and (b) an off-line tracer model described in *Miller and Tegen* [1998]. Each bar is divided into contributions from the lower troposphere (light; surface-720 mb), middle troposphere (darker; 720–39 mb), upper troposphere (light; 390–150 mb), and the lower stratosphere (darkest; 150–10 mb). The size-integrated burden is indicated in the upper right corner.

Despite estimates by *Miller and Tegen* [1998] and *Woodward* [2001], global radiative forcing at the surface remains uncertain due to imprecise knowledge of the dust distribution. Table 1 shows that among current models, estimates of the global dust burden vary by over a factor of two, while the ratio of clay aerosol to larger silt particles varies at least fourfold. We quantify the global sensitivity of the surface forcing to these uncertainties, along with those in the particle optical properties, where there is disagreement among laboratory [*Patterson et al.*, 1977] and in situ measurements [*Kaufman et al.*, 2001; *Sinyuk et al.*, 2003]. While single column models have been used to investigate the forcing sensitivity in the context of a particular regional climate [*Sokolik and Golitsyn*, 1993; *Claquin et al.*, 1998; *Liao and Seinfeld*, 1998], the climate response to dust depends upon the global average of the forcing, or at least the average over the scale of the perturbed circulation. Here, we rank contributions by poorly known aspects of the dust distribution to the global forcing uncertainty. Our calculation of the global sensitivity of surface forcing complements the calculation of TOA sensitivity by *Myhre and Stordal* [2001]. In Section 2, we present our dust distribution, calculated as a radiatively active tracer within the NASA Goddard Institute for Space Studies (GISS) atmospheric general circulation model (AGCM), using a parameterization described by *Tegen and Miller* [1998]. In Section 3, we calculate the surface forcing, and identify aspects of the dust distribution making the greatest contribution to the forcing uncertainty.

[7] Through surface radiative forcing, dust interacts with the hydrologic cycle. Sunlight is reduced beneath the dust layer, which is balanced largely by a reduction of surface evaporation [*Coakley and Cess*, 1985; *Miller and Tegen*, 1998; *Ramanathan et al.*, 2001]. However, we show in Section 4 that while evaporation and precipitation are reduced globally by dust, rainfall increases over deserts—a negative feedback by dust emission to desertification. The global reduction in precipitation increases the dust burden by reducing the efficiency of wet deposition. By comparing the dust distribution computed by the AGCM with and without dust radiative forcing, we calculate this reduction, and its amplification of the dust burden. *Yung et al.* [1996] speculate that the increased dust load during glacial times [*Petit et al.*, 1990; *Biscaye et al.*, 1997; *Reader et al.*, 1999; *Mahowald et al.*, 1999; *Kohfeld and Harrison*, 2001] is due to the weakening of the hydrologic cycle by the colder climate. We estimate to what extent the hydrologic cycle is diminished by dust radiative forcing in present-day and glacial climates. Our conclusions are presented in Section 5.

2. Dust Distribution

[8] Surface radiative forcing by soil dust is calculated by first computing the aerosol distribution using the NASA GISS AGCM [*Tegen and Miller*, 1998]. The distribution of dust depends upon the model circulation, which is perturbed by dust radiative heating, so that the aerosol is a fully interactive part of the AGCM. The parameterization of dust is described in detail by *Tegen and Miller* [1998], and references therein. Here, we summarize the scheme in relation to more recent models. We evaluate the distribution calculated by the model, and identify features that are weakly constrained by the observations that lead to uncertainty in the associated forcing.

[9] The AGCM used to calculate the dust distribution has horizontal resolution of 4° latitude by 5° longitude, with 12 vertical layers extending from the surface to 10 mb. A mixed-layer ocean with prescribed ocean heat transport is coupled to the lower boundary [*Miller et al.*, 1983], so that sea surface temperature can adjust to

Table 2. Global and Annual Average Emission (mg m^{-2} d^{-1}) and Aerosol Load (mg m^{-2}) of Clay and Silt Particles, Along With Their Calculated Aerosol Lifetime (d)

	Emission	Load	Lifetime
Clay	1.9	18.0	9.3
Silt	3.5	10.6	3.0

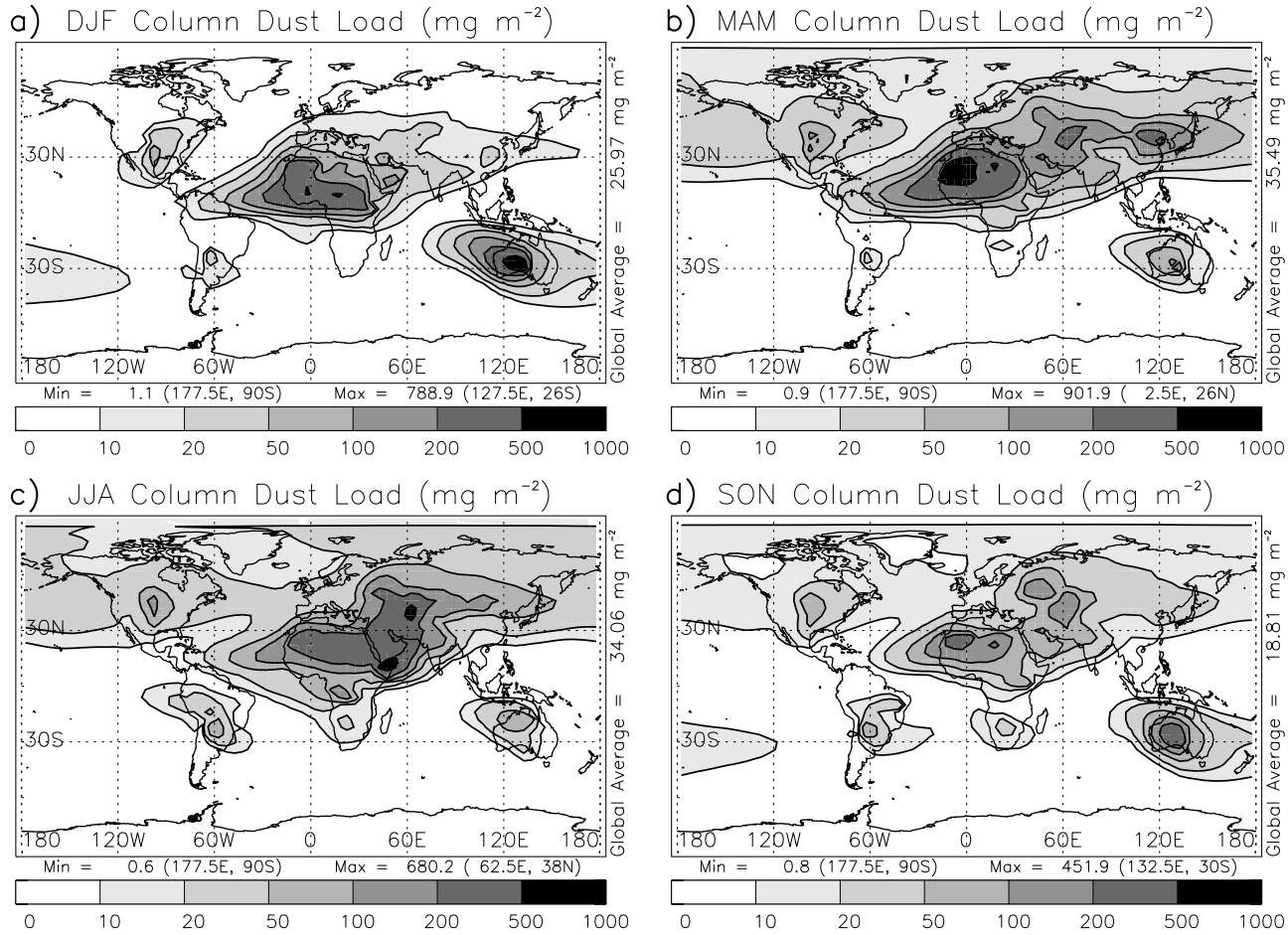

Figure 3. Column average dust load (mg m^{-2}). (a) DJF, (b) MAM, (c) JJA, and (d) SON.

radiative forcing by dust. Tracers (including dust) are advected using a quadratic upstream scheme. This computes not only the tracer value at each grid point but its gradient and curvature, resulting in higher effective resolution of tracers [*Prather*, 1986]. Calculation of realistic dust emission depends upon the model's ability to simulate the observed surface wind and soil moisture. The AGCM surface wind is calculated using similarity theory [*Hartke and Rind*, 1997], with a second-order closure scheme used to relate the interior winds to the surface value [*Mellor and Yamada*, 1982; *Galperin et al.*, 1988]. The model's hydrologic cycle was ranked in the top quartile by the Atmospheric Model Intercomparison Project [*Lau et al.*, 1996].

[10] The model transports four size categories of soil dust, including clay particles (defined by radii <1 μm), and three silt categories. Clay particles settle gravitationally with nearly identical fall speeds, and can be advected to a good approximation as a single size class [*Tegen and Lacis*, 1996].

[11] Calculation of emission depends upon identifying potential source regions and determining whether the meteorological conditions for emission are satisfied. Intuitively, emission should occur over dry regions where there is abundant loose soil vulnerable to wind erosion. In practice, this has led to a number of plausible physical criteria, summarized by *Ginoux et al.* [2001] along with *Zender et al.* [2003b], that lead to markedly different estimates of emission in some regions. Following *Tegen and Fung* [1994], we use the vegetation cover data set compiled by *Matthews* [1983] to allow dust emission in desert, grassland, and shrub regions, where vegetation is low and sparse. Vegetation is fixed, even though *Tegen et al.* [2002] show that Asian dust emission is increased if grass cover emerges only after the onset of spring rains. We also allow emission in dry soils disturbed by agriculture, overgrazing or deforestation [*Tegen and Fung*, 1995; *Tegen et al.*, 1996]. By these criteria, emission can occur potentially over a third of the global land surface. Recent dust models designate "preferred" source regions, where there are fine, erodible particles in abundance, such as the exposed bed of former lakes [*Ginoux et al.*, 2001; *Tegen et al.*, 2002; *Luo et al.*, 2003; *Zender et al.*, 2003a]. Our model does not explicitly include these sources. While their introduction brings the model dust load into better agreement with satellite retrievals in the vicinity of source regions, the large-scale distribution that determines the global forcing is comparatively insensitive [*Zender et al.*, 2003b].

[12] Wind-tunnel measurements suggest that emission occurs when the friction speed (defined as the square-root of the wind stress divided by the air density) exceeds a

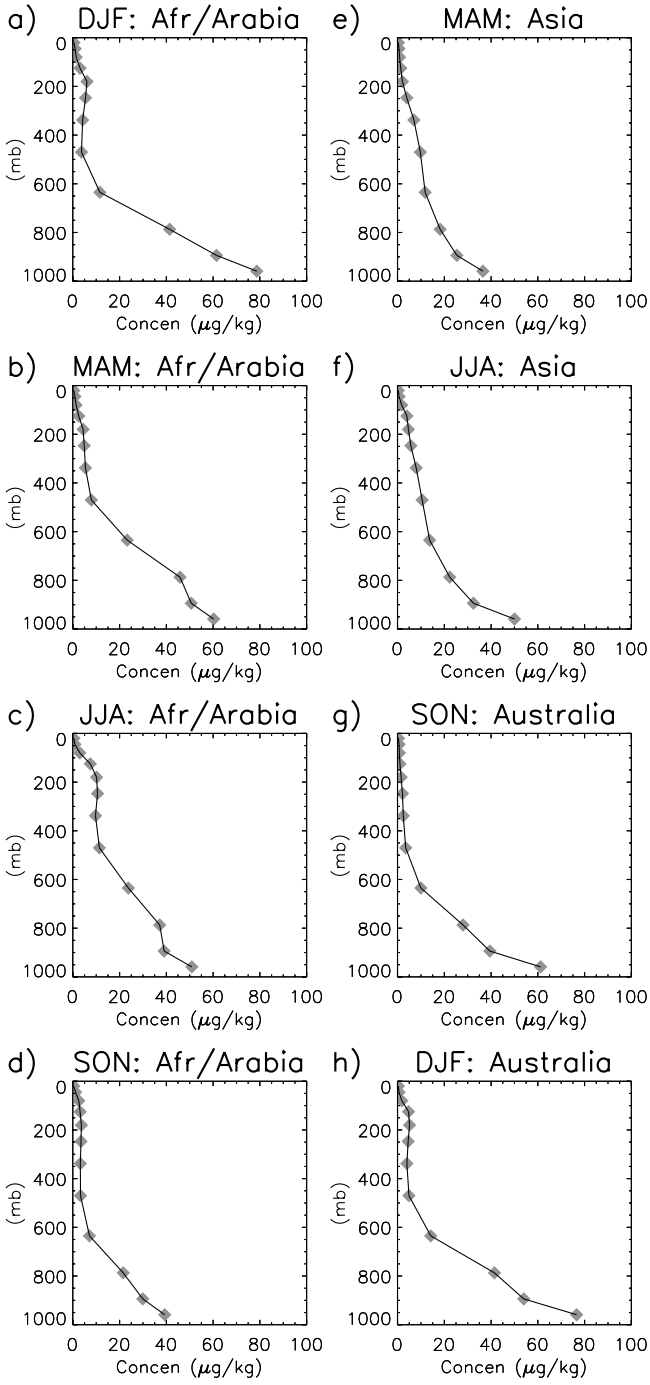

Figure 4. Dust mixing ratio (μg kg^{-1}) over Africa and the Arabian Penisula for (a) DJF, (b) MAM, (c) JJA, and (d) SON. Also for Asia for (e) MAM, (f) JJA and Australia for (g) SON, and (h) DJF. The mixing ratio is averaged within each region where the column dust load exceeds 50 mg m^{-2}.

threshold [*Gillette*, 1978]. The friction speed is related to the surface wind speed by the roughness parameter [*Arya*, 1988]. In the absence of a global data set of surface roughness, whose resolution is comparable to source variations, we calculate emission solely in terms of surface wind speed, a method which has been shown to represent the seasonal pattern of Saharan emission reasonably well [*Marticorena et al.*, 1999]. We assume that saltation is the dominant means of lifting small particles from the surface [*Shao et al.*, 1993], so that the threshold wind speed is interpreted as the value that lifts the larger, saltating particles [*Schulz et al.*, 1998]. We allow the threshold to vary geographically so that emission approximately equals that computed by the off-line transport model of *Tegen and Lacis* [1996], where ECMWF analyzed surface winds with $1\frac{1}{8}^\circ \times 1\frac{1}{8}^\circ$ horizontal resolution were used. Where wind speeds beneath the scale of the AGCM grid box are large, as indicated by the ECMWF analyses, the threshold wind speed is reduced [*Tegen and Miller*, 1998]. The global average threshold (weighted geographically by emission) is 4.5 ms^{-1}, compared to 6.5 ms^{-1} in the off-line model of *Tegen and Fung* [1994].

[13] Dust is removed from the atmosphere by a combination of dry deposition through gravitational settling and turbulence, along with wet deposition, where particles are swept out by precipitation. Gravitational deposition depends upon particle size and is efficient only for the larger silt particles. Wet deposition is proportional to the surface precipitation and scrubs the column to a fixed height that is specified based upon the climatological extent of deep convection [*Tegen and Fung*, 1994]. Table 1 shows that the resulting deposition lifetimes are within the range of recent models [*Ginoux et al.*, 2001; *Tegen et al.*, 2002; *Luo et al.*, 2003; *Zender et al.*, 2003a].

[14] Dust emission within the AGCM, averaged seasonally both for various regions and the entire globe, is shown in Figure 1. Averages are based upon a thirty-one year integration following a nineteen year spin-up, during which time the ocean mixed layer comes into equilibrium with the dust radiative forcing. The global and annual average emission is 1019 ± 54 Tg, slightly smaller than one standard deviation below the total calculated by *Perlwitz et al.* [2001], using an identical model but with prescribed climatological SST as a lower boundary condition. Dust emission is not directly observed, but the

Table 3. Annual and Global Average Radiative Forcing by Dust Aerosols (Wm^{-2}), With the Net Forcing (Positive Downward) Decomposed Into Solar (SW) and Longwave (LW) Contributions

	$0.9 \times \varpi$	$1.0 \times \varpi$	$1.1 \times \varpi$
TOA:			
SW	0.61	−0.33	−0.96
LW	0.15	0.15	0.14
Net	0.76	−0.18	−0.82
Surface:			
SW	−2.65	−1.82	−1.24
LW	0.18	0.18	0.17
Net	−2.47	−1.64	−1.07
Atmos. Heating:			
SW	3.23	1.49	0.28
LW	−0.03	−0.03	−0.03
Net	3.26	1.46	0.25

Forcing is based upon the AGCM dust distribution calculated using optical properties derived from laboratory measurements of far-travelled Saharan dust (the column denoted by $1.0 \times \varpi$). In the columns denoted by $0.9 \times \varpi$ and $1.1 \times \varpi$, forcing is calculated using the same distribution, but assuming more absorbing and more reflecting particles, respectively.

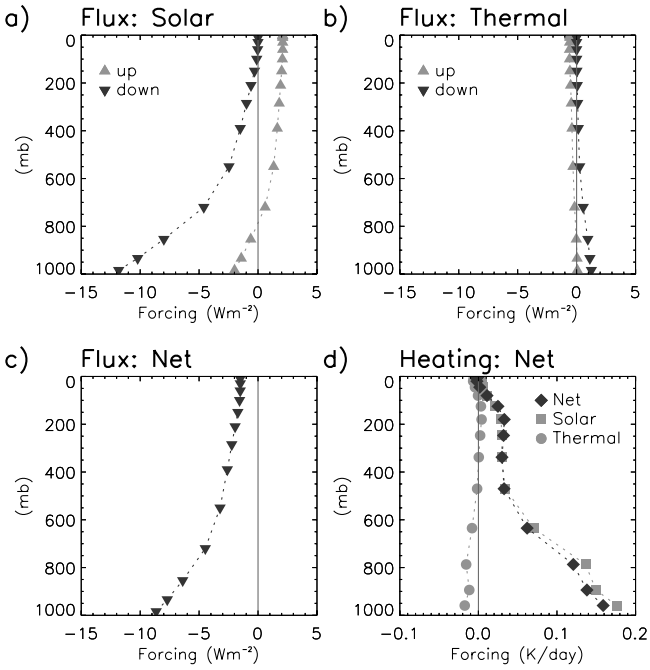

Figure 5. Radiative forcing within the global dust layer, calculated where the column burden exceeds 50 mg m^{-2}. Annual average forcing of the (a) solar, (b) thermal, and (c) net (down minus up, solar plus thermal) fluxes (W m^{-2}). (d) Net radiative heating by dust (K per day).

present model value is among the lower estimates. According to the models listed in Table 1 [*Ginoux et al.*, 2001; *Tegen et al.*, 2002; *Luo et al.*, 2003; *Zender et al.*, 2003a], global, annual emission ranges from 1100 to 1800 Tg for particles smaller than 10 μm. Based upon measurements of ocean deposition, *Duce et al.* [1991] estimate a lower bound of 910 Tg.

[15] According to Figure 1b, global emission is dominated by the Sahara and Sahel in all seasons. The Northern Hemisphere (NH) springtime peak in this region is consistent with observed Sahel visibility [*N'Tchayi Mbourou et al.*, 1997] along with observational estimates of emission in the Western Sahara [*d'Almeida*, 1986]. Emission is also large during the NH spring in Central and East Asia, and during the Southern Hemisphere spring and summer in Australia. While a third of the land surface has the potential to emit dust within the AGCM, two-thirds of the total emission occurs within a few percent of the land area. This emphasizes the localized nature of dust emission [*Goudie and Middleton*, 2001; *Prospero et al.*, 2002]. High winds associated with emission are confined to a few specific regions.

[16] The global dust load is only loosely constrained by observations. While the models of *Ginoux et al.* [2001], *Tegen et al.* [2002], *Luo et al.* [2003], and *Zender et al.* [2003a] reproduce observed surface concentrations [*Prospero*, 1996], along with such measures of column amount as the Aerosol Robotic Network (AERONET) optical thickness [*Holben et al.*, 1998] or the Total Ozone Mapping Spectrometer retrievals [*Herman et al.*, 1997; *Torres et al.*, 2001], global and annual averaged burdens in these models range from 17.4 to 35.9 Tg (Table 1). Our model value of 14.6 Tg is at the low end, raising the possibility that our forcing derived in the next section underestimates the actual value.

[17] The contribution of each size category to our global dust load is shown in Figure 2. While nearly twice as much silt is emitted in comparison to clay (Table 2), the latter dominates the aerosol load. Clay particles are removed from the atmosphere mainly by wet deposition, which is less efficient compared to gravitational and turbulent settling of the larger silt particles. In Table 2, the particle residence time is estimated by dividing the aerosol load by the emission rate. Clay particles reside for nearly 10 days, three times longer than the larger and less buoyant silt particles. Table 1 shows that our particle lifetimes are within the range computed by recent models.

[18] The model size distribution is consistent with that measured a few thousand kilometers downwind of the Sahara, where clay particles are the most prevalent [*Duce*, 1995]. Clay particles also dominate the model distribution over gridboxes where emission is strongest (not shown). This is in contrast to AERONET retrievals [*Ginoux et al.*, 2001; *Ginoux*, 2003], where close to source regions, silt particles make the greatest fractional contribution. Figure 2b shows the size distribution calculated by an off-line transport version of the AGCM's dust parameterization [*Miller and Tegen*, 1998], where the silt burden is 1.4 times that of clay. The peak contribution to the aerosol load comes from the smallest silt category, rather than the largest clay category that makes the greatest contribution in the AGCM. The contrast between the two distributions in Figure 2 is largely due to the planetary boundary layer parameterization used to compute the surface wind speed. Among recent models, the clay fraction of our global burden is large (Table 1), although there is little consensus about the correct value. Because of this disagreement, we consider the sensitivity of the surface forcing to particle size in the next section.

[19] The geographic distribution of the atmospheric dust load is shown in Figure 3. Over Africa, the dust plume swept westward by the Trades is centered at Sahelian latitudes during NH winter and downwind of the Sahara during summer. Dust from Central and East Asia extends over the Pacific during NH spring and summer. These features are qualitatively consistent with AVHRR retrievals of aerosol optical depth [*Husar et al.*, 1997], although the plume of Saharan dust extends insufficiently westward over the Atlantic during NH summer, mainly due to wet deposition by excessive AGCM precipitation along the trajectory (R. Cakmur, personal communication). A quantitative comparison to AVHRR was carried out by *Perlwitz et al.* [2001], using a dust distribution computed by the same AGCM, but with climatological SST rather than the mixed-layer ocean used here as a lower boundary condition. [Despite the different boundary condition, the climatological load of the present model is highly correlated with that of *Perlwitz et al.* [2001], with a median spatial correlation of 0.97 over the twelve months of the annual cycle.] *Perlwitz et al.* [2001] demonstrate that the AGCM generally reproduces the spatial extent of the dust load, although it underestimates the global integral. Despite the global underestimate, the model exceeds the aerosol opti-

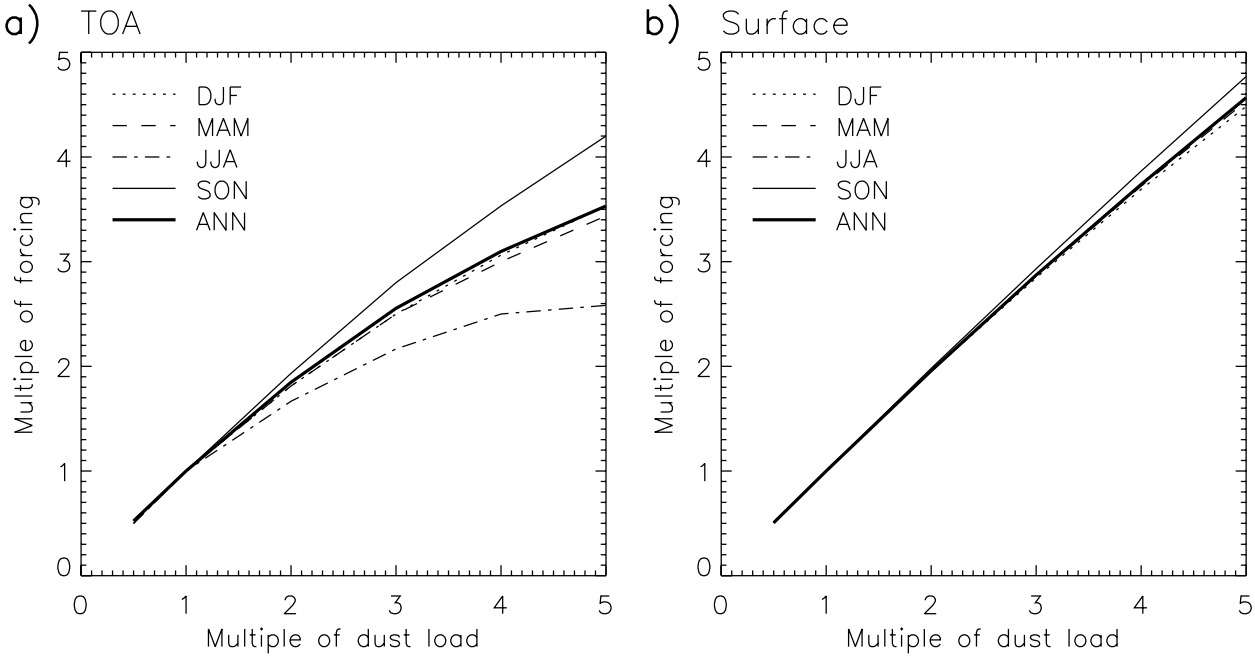

Figure 6. Global and annual average (a) TOA and (b) surface forcing calculated with a rescaled AGCM dust distribution. The distribution is multiplied by a constant (equal to 0.5, 1, 2, 3, 4, and 5) that is independent of location, and the forcing is normalized by its value corresponding to the constant equal to 1.

cal thickness inferred by AVHRR over Australia. We will subsequently calculate the contribution by this region to the global forcing. By using preferred source regions corresponding to dry, topographic depressions, *Ginoux et al.* [2001], *Tegen et al.* [2002], and *Zender et al.* [2003a] simulate Australian emission in better agreement with surface observations, although this agreement may be sensitive to the surface wind analyses used to compute emission [*Luo et al.*, 2003].

[20] The vertical distribution of dust is given by Figure 4, based upon a regional average where the dust load exceeds 50 mg m^{-2} (Figure 3). The African and Asia plumes are arbitrarily divided by the meridian at 25°E poleward of 36°N, and the meridian at 95°E to the south. The mixing ratio falls off rapidly above the surface, although it remains non-negligible in the upper troposphere over Asia during NH spring and summer, and as high as the lower stratosphere during NH summer over Africa and the Arabian penisula.

3. Surface Radiative Forcing

[21] Radiative forcing is calculated using the distribution of dust particles described in the previous section. Per unit mass, extinction by scattering and absorption peaks at a wavelength comparable to the particle size [*Andreae*, 1995], which for clay particles is near the wavelength of maximum solar irradiance. While their nearly identical lifetimes allow them to be transported as a single size category, radiative forcing by clay particles depends upon the precise form of the size distribution within this category. We compute their radiative forcing by subdividing the clay category into four bins, with effective radii of 0.1, 0.2, 0.4, and 0.8 μm, respectively. The subdivision by mass is based upon the distribution of clay particles calculated explicitly by *Tegen and Lacis* [1996]. The effective radius of each silt category is 1, 2, and 4 μm, respectively. The contribution of larger particles to the global forcing is negligible [*Tegen et al.*, 1996].

[22] Radiative fluxes in the GISS AGCM are computed using the single Gauss point doubling/adding algorithm [*Lacis and Mishchenko*, 1995]. The radiative effect of dust is calculated using Mie theory, where particles are treated as homogeneous spheres, and absorption and scattering of radiation at a particular wavelength depend solely upon the index of refraction and particle size. We assume a globally uniform index of refraction, taken from laboratory measurements at infrared [*Volz*, 1973] and solar wavelengths [*Patterson et al.*, 1977] of far-traveled Saharan dust arriving at Barbados. We examine subsequently the forcing sensitivity to changes in the particle optical properties—that result from regional variations in mineralogy, for example.

[23] In the GISS AGCM, aerosol radiative effects at solar and thermal wavelengths are treated separately. Multiple scattering effects are included in the solar calculation. At thermal wavelengths, scattering is small in comparison to absorption, and is neglected [*Tegen and Lacis*, 1996]. *Dufresne et al.* [2002] show that this neglect reduces the thermal contribution to forcing at TOA by half, although the reduction at the surface (and to radiative forcing within the atmosphere) is <15%. Because the thermal contribution to global forcing will be shown to

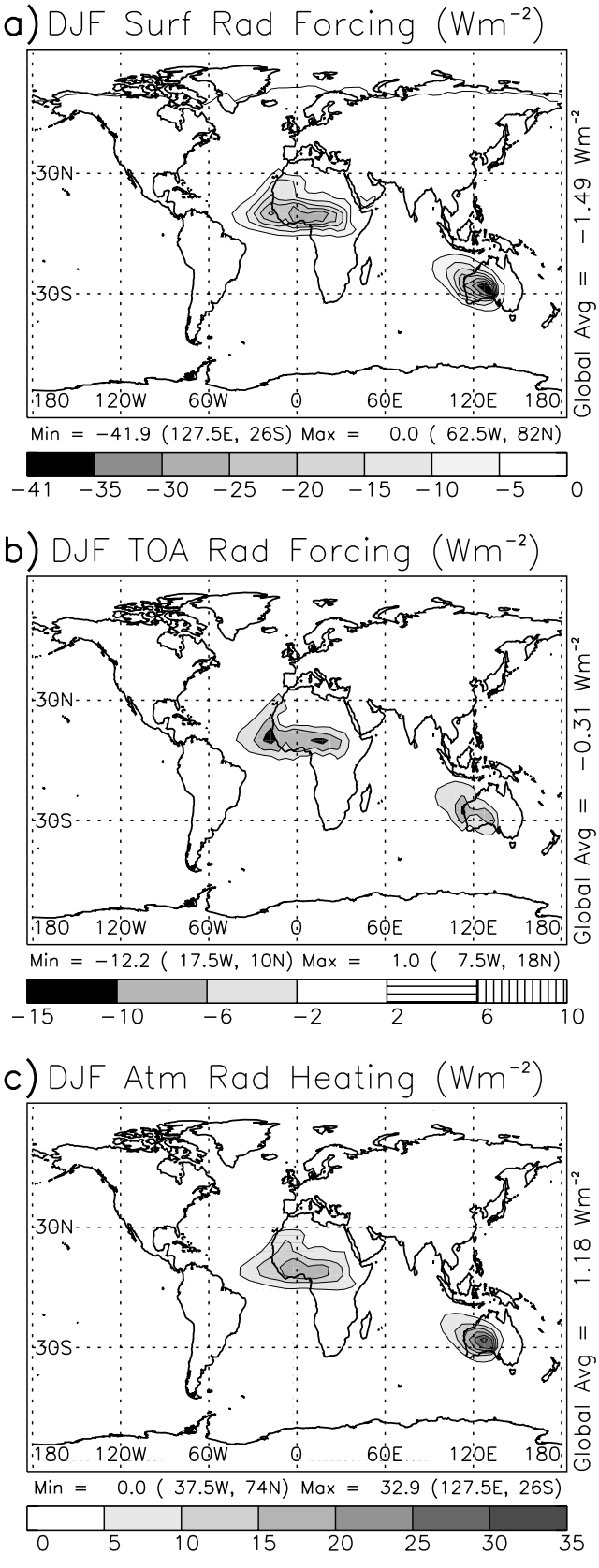

Figure 7. DJF dust radiative forcing at the (a) surface and (b) top of the atmosphere. (c) Radiative heating of the atmosphere by dust (i.e., the difference between the surface and TOA values) in W m^{-2}.

be relatively small, this neglect has little effect upon our conclusions.

[24] Dust radiative forcing is defined as the perturbation to the radiative budget by dust prior to any response by the climate. We calculate the forcing by first integrating an AGCM without dust through one annual cycle. The model temperature, humidity, and cloud cover are archived every five hours, and then used to calculate radiative fluxes with and without the climatological dust distribution described in the previous section. The forcing is defined as the flux difference between the two calculations. The forcing is sensitive to the albedo of the column underlying the dust layer, which requires an accurate simulation of clouds. The GISS AGCM has been shown to be one of the most accurate in model comparisons to observed cloudiness and its variability [*Weare et al.*, 1995], along with cloud forcing [*Cess et al.*, 1995].

[25] Although the forcing is strictly defined prior to any climate response, the distinction between the two is imprecise. The climate is altered by the presence of dust, whose geographic distribution and associated forcing depend upon the climate. One example of this interaction is the roughly 15% reduction of the dust load by the climate response to dust radiative forcing [*Perlwitz et al.*, 2001]. Because this reduction is a small compared to the uncertainty of the load, we ignore this ambiguity in the forcing calculation.

[26] As a baseline for the sensitivity calculation, we compute the global and annual average radiative forcing (Table 3, center column). Dust attenuates the incident solar flux through a combination of absorption and reflection. At thermal wavelengths, dust absorbs radiation from the surface, reducing outgoing emission at the top of the atmosphere, while increasing the flux back toward the ground. Because most dust particles are small compared to thermal wavelengths—especially beyond a few hundred kilometers from the source region [*Duce*, 1995]—solar forcing dominates the thermal component on a global scale, even though dust particles are highly absorbing at longer wavelengths [*Sokolik and Toon*, 1999]. The net forcing at the surface is −1.64 Wm^{-2}. At TOA, the net forcing is negative but nearly zero; negative forcing by shortwave reflection is almost completely offset by absorption at solar and thermal wave-

Table 4. Contribution of the NH African/Arabian, Asian, and Australian Source Regions to the Total Global Average Forcing by Dust Aerosols (Wm^{-2})

	DJF	MAM	JJA	SON	ANN
Surface:					
NH Africa/Arabia	−0.75	−1.18	−1.08	−0.38	−0.85
Asia	−0.03	−0.47	−0.60	−0.16	−0.32
Australia	−0.44	−0.07	−0.04	−0.22	−0.19
Other	−0.27	−0.25	−0.33	−0.27	−0.28
Total	−1.49	−1.97	−2.05	−1.04	−1.64
TOA:					
NH Africa/Arabia	−0.22	−0.15	−0.04	−0.06	−0.12
Asia	0.00	−0.02	−0.02	−0.03	−0.01
Australia	−0.09	−0.02	−0.02	−0.05	−0.04
Other	−0.00	−0.01	−0.04	−0.02	−0.02
Total	−0.32	−0.16	−0.12	−0.15	−0.18

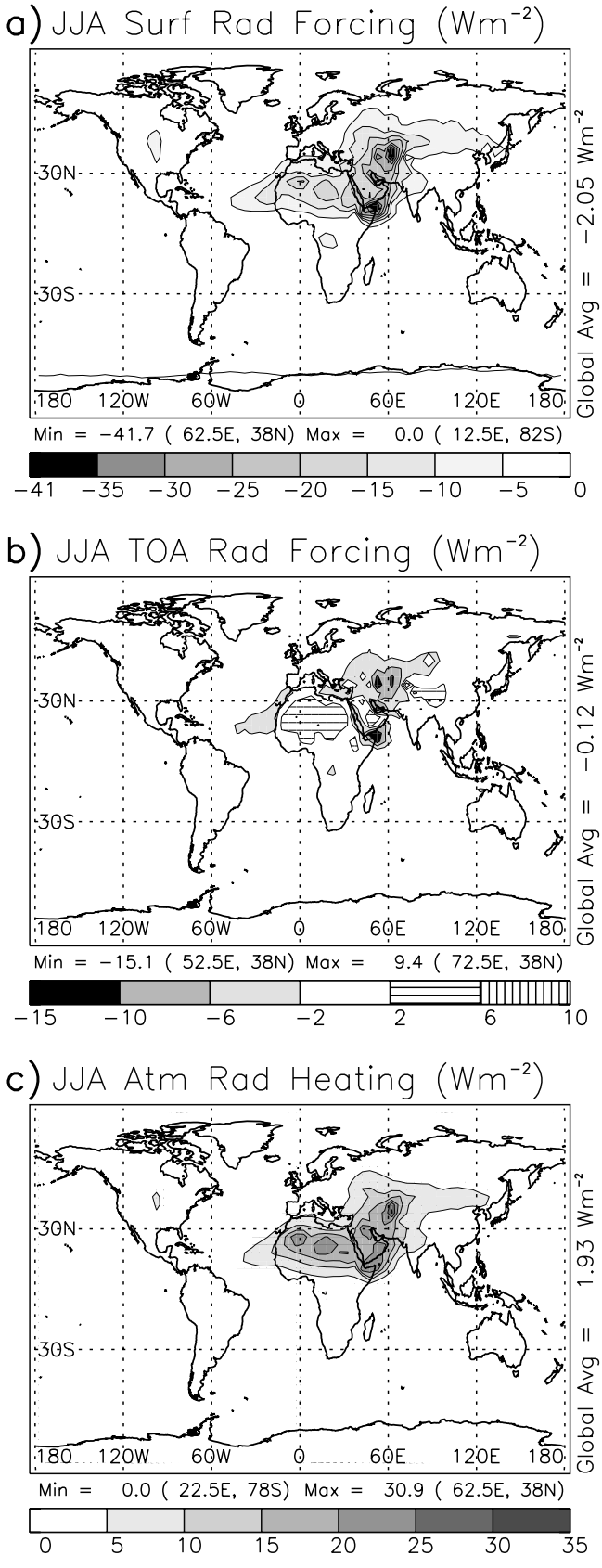

Figure 8. Same as Figure 7 but for JJA.

lengths. The difference between the surface and TOA forcing is proportional to diabatic heating within the atmosphere. This heating, corresponding to roughly 0.01 K per day, is dominated by the solar component. This is a small offset of the tropic-wide longwave cooling rate, whose magnitude of roughly 1 K per day [*Holton*, 1992] determines the strength of the large-scale tropical circulation [*Pierrehumbert*, 1995]. However, within the dust layer, defined as the region where the column burden exceeds 50 mg m^{-2} (c.f. Figure 3), the heating rate is on the order of 0.1 K per day (Figure 5d), offsetting by roughly 10% the tropic-wide cooling. The heating extends throughout the troposphere, despite the concentration of dust near the surface. The extension of the heating to well above the dust layer is partly due to decreasing density and thermal inertia with height, as well as reflection of sunlight at the top of the dust layer, which reduces the downward flux and associated forcing below. Given the small TOA forcing and comparatively large surface value, the effect of dust is to displace radiative heating from the surface into the atmosphere [*Miller and Tegen*, 1999; *Ramanathan et al.*, 2001].

[27] The model's aerosol burden is at the low end of current estimates. The burdens listed in Table 1 are larger by as much as a factor of two and a half. To examine the sensitivity of our global forcing estimate to a higher aerosol amount, we increased our baseline dust load (Figure 3) by a globally uniform factor and recomputed the forcing. Figure 6 shows the global average surface and TOA forcing, normalized by their baseline values (Table 3, center column), for global loads ranging from half the baseline estimate to five times this amount. To a good approximation, the forcing is linear in this range for all seasons. If the present-day global burden is as large as calculated by *Ginoux et al.* [2001], then the actual surface forcing is over twice our model's estimate. In this case, the atmospheric radiative heating within the dust layer is as large as a quarter of the tropical radiative cooling rate.

[28] Figures 7a and 8a show the geographic distribution of surface forcing for NH winter and summer, respectively. Regional variations in the surface forcing largely follow variations in the column dust load. Where the dust layer is optically thick, the surface forcing is generally the most negative. The TOA forcing is modulated by regional variations in the planetary albedo (not shown), which measures the combined reflectivity of the atmospheric column and underlying surface [*Andreae*, 1995]. During NH winter (Figure 7b), the negative forcing is largest in magnitude where the dust cloud extends over the dark, verdant coast of the Gulf of Guinea and the eastern Atlantic. During NH summer (Figure 8b), when the plume is centered farther north over the comparatively bright Sahara, the TOA forcing in this region changes sign to positive. Because the forcing at TOA is small compared to the surface value, regional variations in atmospheric radiative heating generally follow surface variations, which in turn are dominated by regional variations in the column dust load (Figures 7c and 8c).

[29] Our model's overestimate of Australian emission, noted in the previous section, may bias our estimate of the global forcing. To quantify this effect, we calculate the

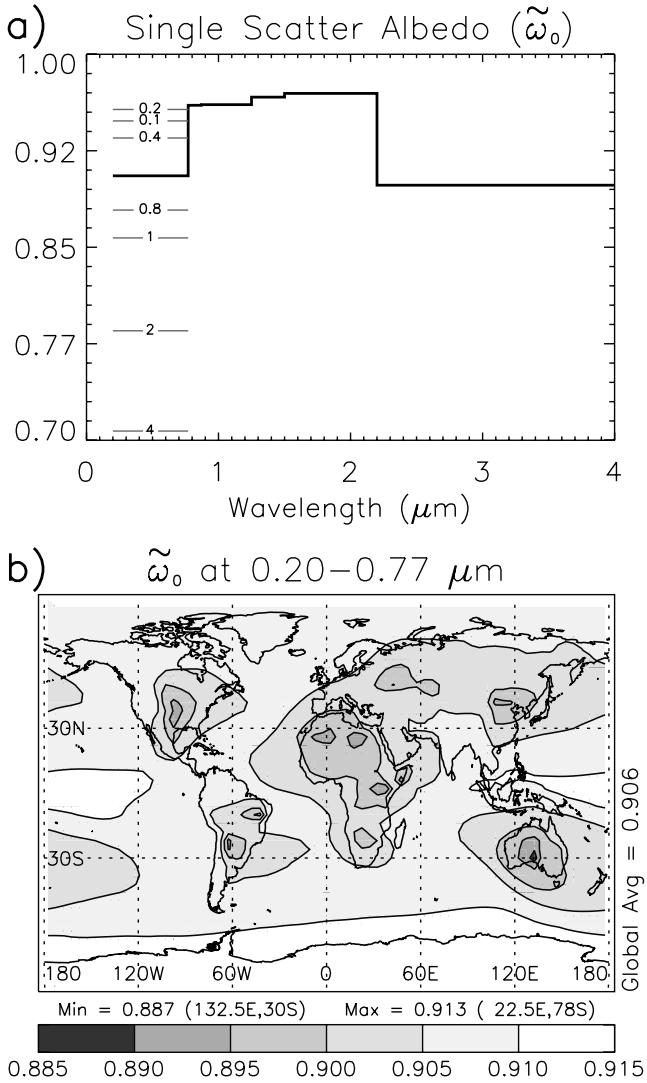

Figure 9. (a) Annual and global average of the bulk single scatter albedo ϖ_0 for dust particles, for the six spectral bands used in the calculation of solar radiative forcing. The single scatter albedo is computed for each month as the ratio of the column scattering extinction and the column total extinction. Also shown for the shortest solar band (0.20–0.77 μm) is the single scatter albedo for each individual model size category, denoted by its effective radius. (b) Geographic distribution of the annual average bulk single scatter albedo in the 0.20–0.77 μm band.

contribution to the forcing by each source region (Table 4). The regions are demarcated using the 10 mg m^{-2} contour (Figure 3). The Australian plume is spatially distinct at this threshold. We divide the Asian and African/Arabian plumes as in the previous section (Figure 4). The downstream boundary of the Asian plume is set at 90°W, and African dust is distinguished from sources to the west using the minimum in dust load over the Atlantic. Because dust from each source region extends beyond these boundaries, the regional contribution listed within the table is an underestimate. However, for the case of Australian dust, we found that the TOA value is insensitive to thresholds below 20 mg m^{-2}, suggesting that this underestimate is slight. According to Table 4, Australian dust contributes just over ten percent of the global forcing at the surface. The contribution to the global TOA value is larger (yet still under a quarter) in part because forcing beneath the extensive Asian plume largely cancels due to the compensating albedo effect of dark ocean and bright clouds beneath its trajectory. Even if the actual Australian emission were half the model value, our global forcing estimates would be only slightly reduced.

[30] Forcing has been calculated assuming a uniform index of refraction for all source regions, based upon laboratory measurements of Saharan dust collected at Barbados [*Volz*, 1973; *Patterson et al.*, 1977]. These particles consist mainly of clay and quartz, with enhanced solar absorption due to trace amounts of the iron oxide hematite [*Chester and Johnson*, 1971; *Volz*, 1973]. Because Africa is the dominant source of dust particles, the optical properties of far-traveled Saharan dust are a reasonable first approximation for representing the global aerosol load. This idealization is especially attractive because of the computational cost of four tracer variables needed to represent the size distribution of each additional mineral type.

[31] Nonetheless, other source regions have distinct optical properties [*Sokolik et al.*, 1993], and downwind of the Sahara, variations in aerosol mineralogy are well-known [*Carlson and Prospero*, 1972]. Within the aerosol plume, minerals concentrated in larger particles settle out first [*Claquin et al.*, 1999]. The remaining particles are coated with sulfates as they pass through polluted air [*Dentener et al.*, 1996; *Trochkine et al.*, 2003], and water where clouds form within the aerosol layer [*Sokolik et al.*, 1993]. Both coatings reduce solar absorption. In situ Sun photometer and satellite measurements suggest that solar absorption by Saharan dust is smaller than the laboratory measurements we adopt for our optical properties [*Patterson et al.*, 1977; *Kaufman et al.*, 2001; *Sinyuk et al.*, 2003]. To quantify this discrepancy in our model, we compute the ratio of the scattering extinction to the total extinction, creating a bulk single scattering albedo ϖ_0, which varies inversely with particle absorption. Figure 9a shows the global and annual average of ϖ_0 for the six solar wavelength bands within which dust radiative forcing is calculated. Also shown for the shortest band is the single scatter albedo for each individual size category. The bulk single scatter albedo lies near the value corresponding to the predominant particle size (Figure 2a). Because we assume a globally uniform index of refraction, geographic variations in the bulk single scatter albedo result solely from evolution of the particle size distribution downwind of the source. Figure 9b shows that absorption decreases downwind due to sedimentation of the larger particles. We compare our bulk single scatter albedo to AERONET measurements taken downwind of the Sahara at Capo Verde during NH summer [*Kaufman et al.*, 2001]. At this location, the model ϖ_0 is just over 0.90 in the spectral band between 0.20 and 0.77 μm (Figure 9b). The AERONET values at comparable optical thicknesses are 0.905 at 0.44 μm and 0.935 at 0.67 μm with an estimated uncertainty of 0.02.

While our model is marginally in agreement if the measurement uncertainty is taken into account, this agreement may result from our large fraction of clay aerosol. Were our size distribution weighted toward larger particles, as in some models (Table 1), the excess absorption with respect to AERONET would be larger (Figure 9a).

[32] Given the global variations in particle mineralogy, along with addition of surface coatings along their trajectory, we calculate the forcing sensitivity to variations in the optical properties. We carry out two additional experiments where the particle single scattering albedo ϖ (equal to the ratio of scattering to total extinction for a single particle) is either increased or else decreased by 10%. In either case, total extinction, corresponding to scattering plus absorption, is held constant, and ϖ is never allowed to exceed unity. A 10% increase in ϖ, corresponding to an increase in scattered radiation at the expense of absorption, might represent dust particles comprised solely of clay or quartz, whose solar absorption is nearly zero. Conversely, a 10% decrease in ϖ can represent Saharan particles whose absorptivity is increased by the aggregation of a small amount of additional hematite [*Sokolik and Toon*, 1999]. Note that a 10% increase or decrease is within the range measured globally [*Sokolik et al.*, 1993], and used in aerosol radiation models [*Sokolik and Toon*, 1996]. This variation also bounds the reduction of solar absorption inferred by *Kaufman et al.* [2001] and *Sinyuk et al.* [2003].

[33] The sensitivity of the global and annual average forcing to particle absorption is given by Table 3. The sensitivity of the forcing is large in comparison to the modest changes in the single scattering albedo. For example, the 10% decrease in ϖ results in a 50% increase in the magnitude of the surface forcing, while the forcing at TOA even changes sign. This large sensitivity is due to the domination of the solar forcing over the longwave component. At solar wavelengths, absorption by far-traveled Saharan dust is small, and ϖ is near 0.9 (Figure 9a). Thus a 10% increase reduces particle absorption (proportional to $1 - \varpi$ for ϖ near unity) to nearly zero, while a corresponding decrease doubles the absorption. In contrast, ϖ at thermal wavelengths is closer to 0.5, so that a 10% change has little effect.

[34] Column heating by dust shows a similarly large sensitivity to the particle absorption. Figures 10 and 11 show vertical profiles of the forcing as perturbations to the net flux (in Wm^{-2}) and diabatic heating (in K per day), respectively. In all regions, the heating shows the same sensitivity as the surface forcing, doubling for a 10% reduction in ϖ. For more absorbing particles, the heating rate ranges from 0.2 to 0.3 K per day, even in the upper troposphere. Again, this is a non-negligible offset to the tropical radiative cooling rate of 1 K per day [*Holton*, 1992].

[35] The forcing is also uncertain as a result of the contrasting size distributions calculated by current models (Table 1, Figure 2), where the ratio of silt particles to clay varies over a factor of four. We calculate the sensitivity of the surface forcing to particle size by computing the forcing for each size category separately. This decomposition assumes that the total forcing is equal to the sum of the contributions from each category. In fact, the sum of the forcings calculated separately slightly exceeds the forcing of the entire size distribution (Table 5). Taken together, each size category reduces the radiation incident upon other size particles. However, for the present-day dust load, this

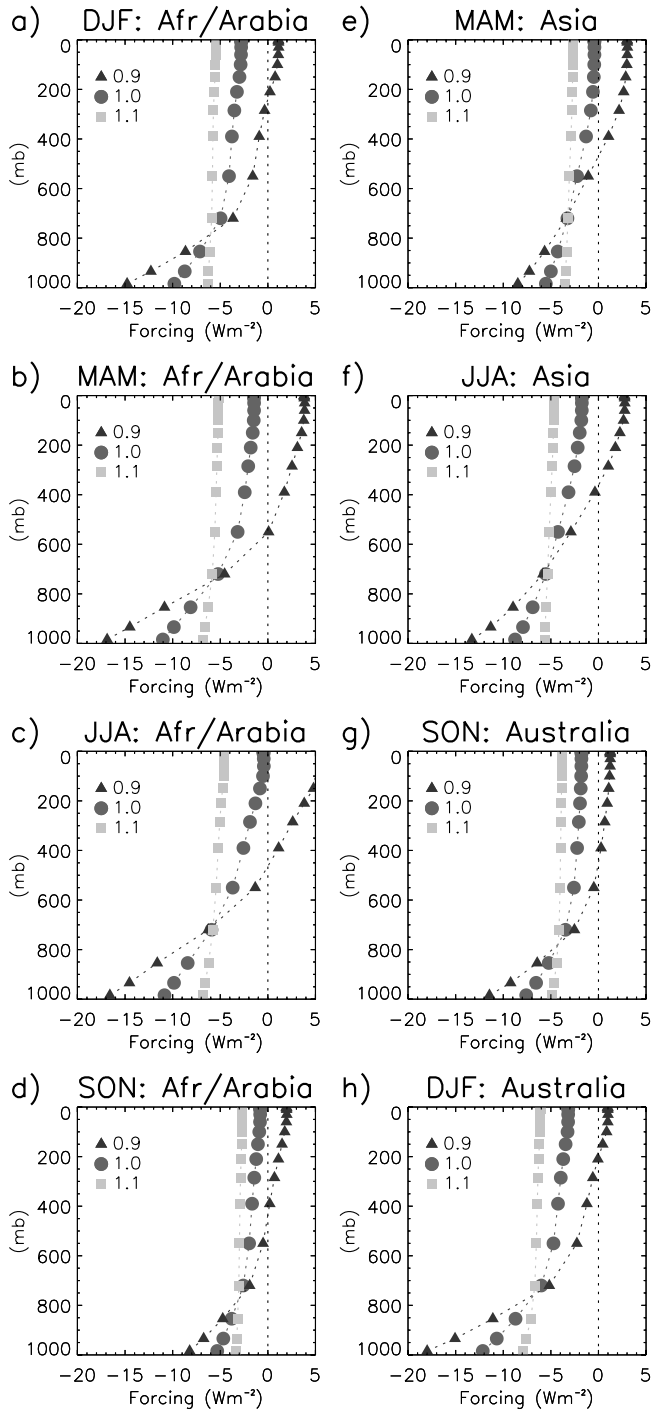

Figure 10. Dust radiative forcing (Wm^{-2}) over Africa and the Arabian Penisula for (a) DJF, (b) MAM, (c) JJA, and (d) SON. Also for Asia for (e) MAM, (f) JJA and Australia for (g) SON, and (h) DJF. The forcing is averaged within each region where the column dust load exceeds 50 mg m^{-2}. Circles correspond to far-travelled Saharan dust ($1.0 \times \varpi$), triangles for more absorbing particles ($0.9 \times \varpi$), and squares for more reflecting particles ($1.1 \times \varpi$).

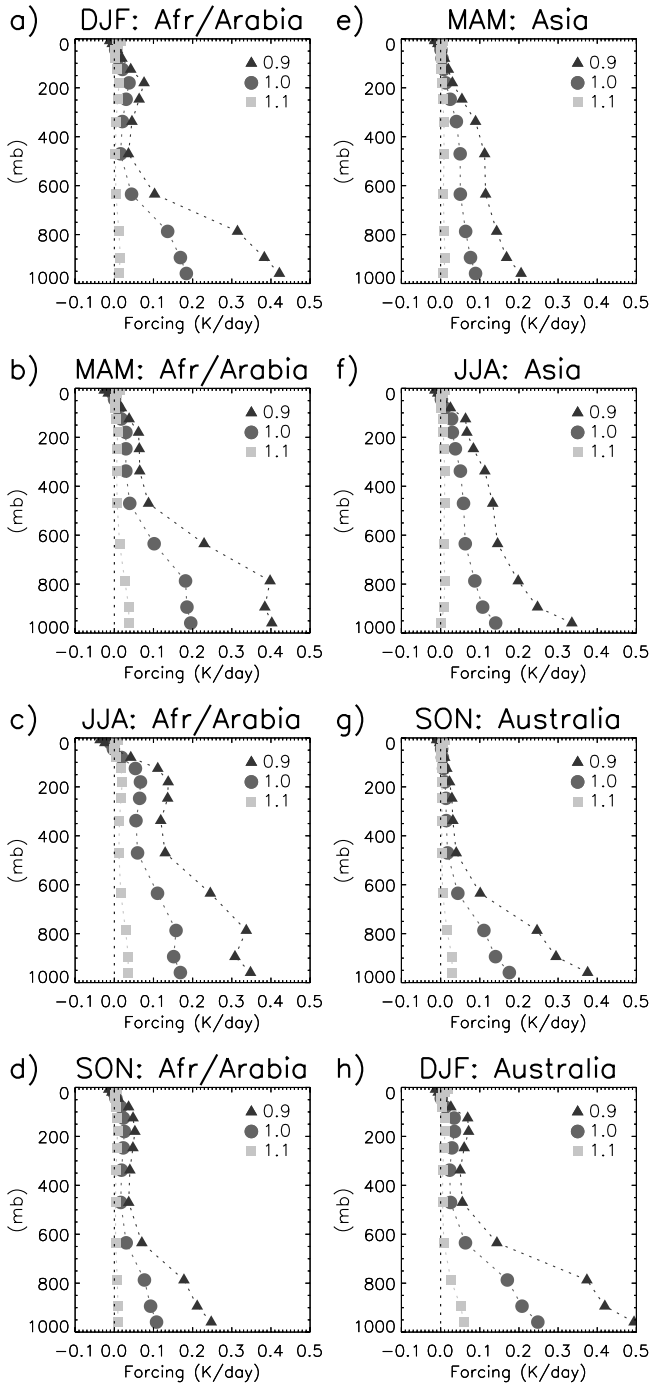

Figure 11. Same as Figure 10 but for radiative heating of the atmosphere by dust (K per day).

difference is very small—a result of the modest magnitude of the present-day dust burden.

[36] The contribution of each size category to the global and annual forcing is shown in Figure 12. The contribution reflects the global abundance of each size category (Figure 2), along with the efficiency of forcing by each category per unit mass—denoted in Figure 13 by diamonds for the current model distribution (Figure 2a) and by crosses for the distribution used by *Miller and Tegen* [1998] (Figure 2b). The similar estimates of forcing per unit mass for the two size distributions, despite different geographical distributions, suggests that this quantity is robust. According to Mie theory, extinction by a single particle is negligible at wavelengths larger than the particle radius, but is roughly constant for shorter wavelengths [*van de Hulst*, 1981]. Moreover, the number of particles decreases per unit mass of aerosol as the radius increases. Thus solar forcing per unit mass peaks for particles with radii comparable to the wavelength of maximum solar irradiance (around 0.5 μm), and thermal forcing increases slowly with particle size for the size range considered here. This accounts for the forcing efficiency shown in Figure 13. At TOA, where solar absorption and reflection make offseting contributions to the forcing, thermal forcing by larger particles can exceed the solar residual to create net positive forcing. In contrast, solar absorption and reflection both create negative forcing at the surface, and the compensating positive forcing at thermal wavelengths is relatively small, even for larger particles. Because of this cooperation, the sign of the forcing is less sensitive to the size distribution at the surface than at TOA.

[37] To estimate the effect of current uncertainties in the size distribution upon the global forcing, we take two size distributions with identical total loads but varying ratios of silt to clay, and multiply the mass of each size category by the forcing per unit mass computed by the AGCM (Figure 13, diamonds). The first size distribution is taken from the AGCM (Figure 2a), and has a ratio of silt to clay aerosol of 0.59. The second size distribution has a ratio of 1.41, and is taken from Figure 2b [*Miller and Tegen*, 1998]. The latter ratio is similar to that computed by *Ginoux et al.* [2001], whose distribution compares well with that retrieved by AERONET. These two ratios of silt to clay are representative of the range among models listed in Table 1. The forcing is listed in Table 6. As the silt burden increases, both the TOA and surface forcing tend toward positive values due to the longwave effect of the larger silt particles. However, despite the large increase in silt fraction, the surface forcing and atmospheric radiative heating remain within ~10% of the value calculated from the AGCM distribution.

4. Dust Forcing of the Hydrological Cycle

[38] In a radiative equilibrium atmosphere, negative forcing at the surface by dust is balanced by a reduction in upward thermal radiation, caused in part by a decrease in ground temperature. The effect of atmospheric dynamics is

Table 5. Global and Seasonal Average Radiative Forcing Calculated by the Baseline Experiment and the Sum of the Forcings for Each Size Class Calculated Separately

	DJF	MAM	JJA	SON	ANN
TOA:					
Baseline	−0.32	−0.16	−0.12	−0.15	−0.18
Sum	−0.33	−0.17	−0.13	−0.16	−0.20
Surface:					
Baseline	−1.49	−1.97	−2.05	−1.04	−1.64
Sum	−1.52	−1.99	−2.07	−1.05	−1.66

to allow the surface to respond alternatively by reducing its turbulent fluxes of sensible and latent heat into the atmosphere. The latter reduces precipitation [*Coakley and Cess*, 1985; *Miller and Tegen*, 1998]. In this section, we show that despite its global decrease, precipitation increases locally over arid regions that are sources of dust. We also show that the global reduction in precipitation by dust radiative forcing reduces the efficiency of wet deposition, which acts as a positive feedback upon the dust load. Finally, we estimate the importance of this feedback for the present-day and glacial climates.

[39] The effect of dust upon climate is assessed by comparing two experiments with the mixed-layer AGCM: one where dust alters the model radiative fluxes (and whose dust distribution and forcing were described in the previous sections), and one where radiative forcing by dust is omitted. More precisely, the effect of dust upon a variable is defined as the difference between the variable's climatological values in the two experiments, where averages are constructed over the final thirty-one years of each simulation, following a nineteen year spin-up. (For radiative fluxes, the effect is this difference minus the forcing.) Because the surface forcing is especially sensitive to absorption by the dust particles, we do two additional experiments, where the particle single scatter albedo is increased or else decreased by 10%. Assessing the effect of dust by contrasting experiments with and without its radiative forcing is similar to the study of *Miller and Tegen* [1998]. However, in that study, the dust distribution was prescribed externally. Here, the dust distribution responds to the climate anomalies it forces, allowing feedbacks upon the dust load resulting from its own radiative forcing.

[40] For each experiment, the surface energy balance is written as:

$$R_{SW} = R_{LW} + LE + S, \tag{1}$$

where R_{SW} is the net shortwave radiation into the surface, R_{LW} is the net longwave radiation from the surface into the atmosphere, LE is the turbulent flux of latent heat leaving the surface, equal to the latent heat of vaporization times the evaporation rate, and S is the turbulent sensible heat flux into the atmosphere. If we perturb the surface by adding radiative forcing $\mathcal{F}_{SRF}$ due to dust, then the budget of the response (denoted by δ) is:

$$\mathcal{F}_{SRF} + \delta R_{SW} = \delta R_{LW} + \delta(LE) + \delta S. \tag{2}$$

(Note the distinction between the surface radiative forcing $\mathcal{F}_{SRF}$ — calculated in the absence of any climate response to dust, as in the previous section—and the surface radiative flux anomaly $\mathcal{F}_{SRF} + \delta R_{SW} - \delta R_{LW} \equiv \delta R_{SRF}$, which is computed allowing the climate of the AGCM with dust to respond to its radiative forcing.) For the sake of discussion, we assume that the forcing is entirely at solar wavelengths, and that the radiative response is restricted to thermal wavelengths. (We examine the validity and consequence of these approximations below.) Then:

$$\mathcal{F}_{SRF} = \delta R_{LW} + \delta(LE) + \delta S, \tag{3}$$

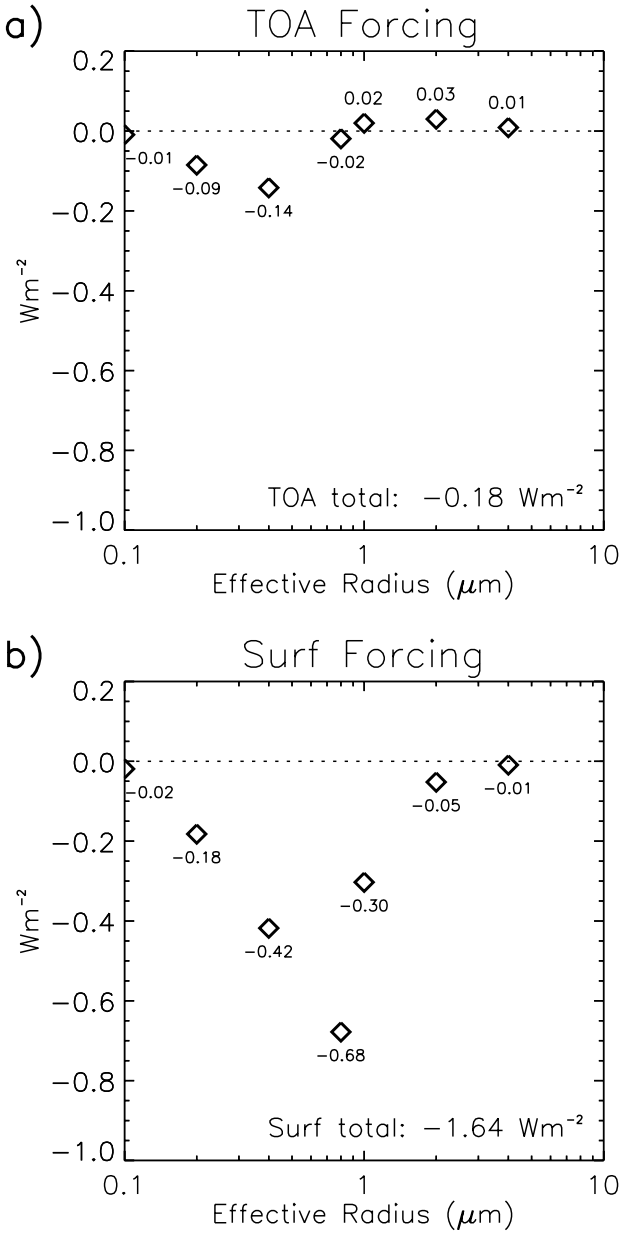

Figure 12. Contribution by each particle size category to the global and annual average dust radiative forcing (Wm^{-2}) at (a) TOA, and (b) the surface. The total indicated in each panel refers to the forcing calculated with the entire size distribution and is slightly less than the sum of the forcings calculated separately for each size class.

where the surface forcing $\mathcal{F}_{SRF}$ is negative as calculated in the previous section. Each of the surface fluxes on the left-hand side of (3) is shown in Figure 14. The global average response of the surface fluxes is given by Table 7 (center column). On a global scale, dust radiative forcing at the surface is balanced predominately by a reduction in the latent heat flux, and secondarily, by the sensible heat flux. The reduction in the latent heat flux is largest over oceanic regions downwind of dust source regions—such as the eastern subtropical Atlantic, the Arabian Sea, and the

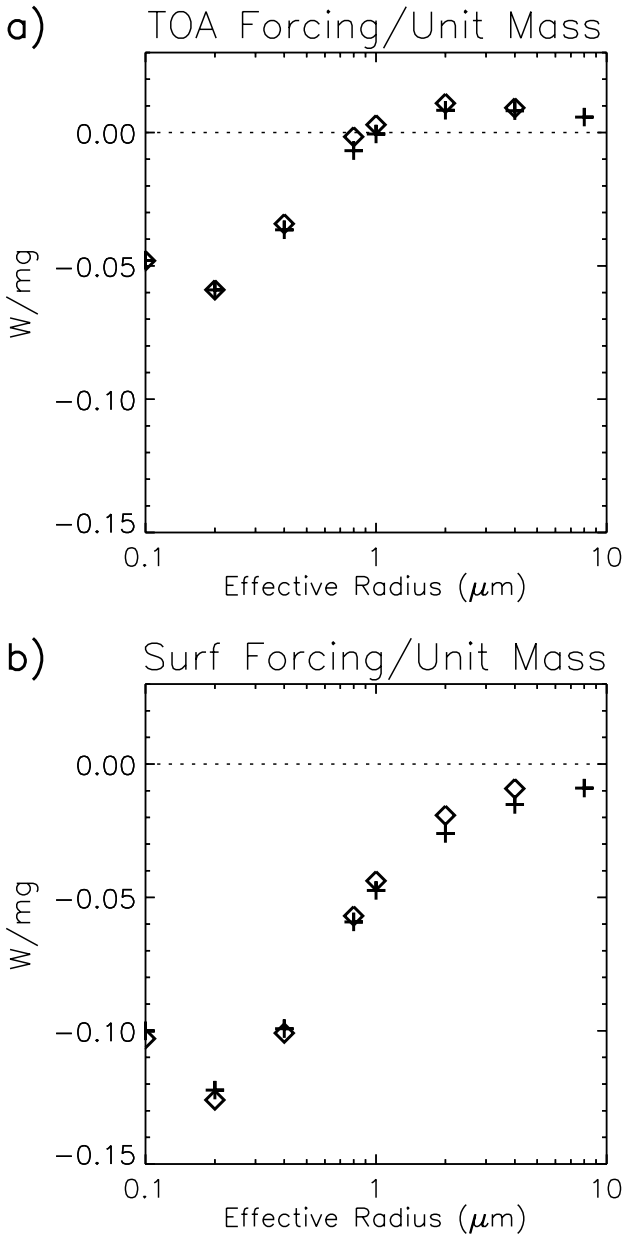

Figure 13. (a) TOA and (b) surface forcing per unit mass of dust for each size category in W mg^{-1}, computed by dividing the forcing (Figure 12) by the dust load (Figure 2) for each size category. The diamonds denote AGCM values; crosses denote values calculated with the dust distribution of *Miller and Tegen* [1998].

southeast Indian Ocean—along with continental areas with abundant soil moisture, such as the West African coast. In comparison to the anomalous turbulent fluxes, the direct radiative response through the net upward longwave flux is small. Our attribution of the longwave anomaly as a response to dust assumes that the surface longwave forcing is negligible. While this may not be the case near source regions [*Claquin et al.*, 1998], where the fraction of large particles is greatest, it is approximately true over the global extent of the dust layer. The small, positive longwave forcing, indicated in Table 3, means that the actual surface longwave response is only slightly greater in magnitude than the anomaly listed in Table 7.

[41] Although the surface latent heat flux is reduced by dust [*Coakley and Cess*, 1985; *Miller and Tegen*, 1998], this reduction is smallest for the most absorbing particles (Table 7). This may seem counterintuitive, because the magnitude of surface radiative forcing increases sharply with particle absorption (Table 3). The explanation is that over desert regions, such as the Sahara and Mojave, the surface latent heat flux is increased by dust (Figure 14a), despite the reduction of incident sunlight. This evaporative increase is largest for the experiment with the most absorbing particles (Figure 15c).

[42] The evaporative increase is associated with the extension of the ITCZ into the western Sahara as particle absorptivity increases (Figures 16 and 17b). In the absence of dust, diabatic heating in this region is dominated by longwave cooling, and is balanced by adiabatic subsidence. Ascent and precipitation occur when radiation absorbed within the aerosol layer is large enough to change the sign of the diabatic heating [*Menon et al.*, 2002].

[43] The anomalous diabatic heating, integrated over an atmospheric column within the dust layer, is given by:

$$\delta H \equiv \mathcal{F}_{TOA} - \mathcal{F}_{SRF} + \delta R_{TOA} - \delta R_{SRF} + \delta LP + \delta S. \quad (4)$$

where $\mathcal{F}_{TOA}$ and δR_{TOA} are the forcing and radiative response at TOA, respectively, and P is the column precipitation. We apply the anomalous surface energy balance (2) to write:

$$\delta H \equiv \mathcal{F}_{TOA} + \delta R_{TOA} + \delta L(P - E). \quad (5)$$

Over the desert, $\mathcal{F}_{TOA}$ is positive (Figures 7a and 8a) and makes its largest contribution to δH, due to the bright underlying surface compared to oceanic or vegetated regions. Moreover, the TOA forcing is largest for the experiment with increased particle absorption.

[44] Precipitation in response to dust radiative forcing is also favored over deserts and dry continental interiors by the

Table 6. Global and Annual Average Radiative Forcing by Dust Aerosols (Wm^{-2}) for Different Ratios of Silt to Clay Aerosol

	Silt/Clay = 0.6	Silt/Clay = 1.4
TOA:		
Clay	−0.26	−0.21
Silt	0.06	0.05
Total	−0.20	−0.16
Surface:		
Clay	−1.30	−0.84
Silt	−0.36	−0.62
Total	−1.66	−1.47
Atmos. Heating:		
Clay	1.04	0.63
Silt	0.42	0.67
Total	1.46	1.31

The forcing is calculated by multiplying the mass corresponding to each category by the global and annual average forcing per unit mass shown in Figure 13.

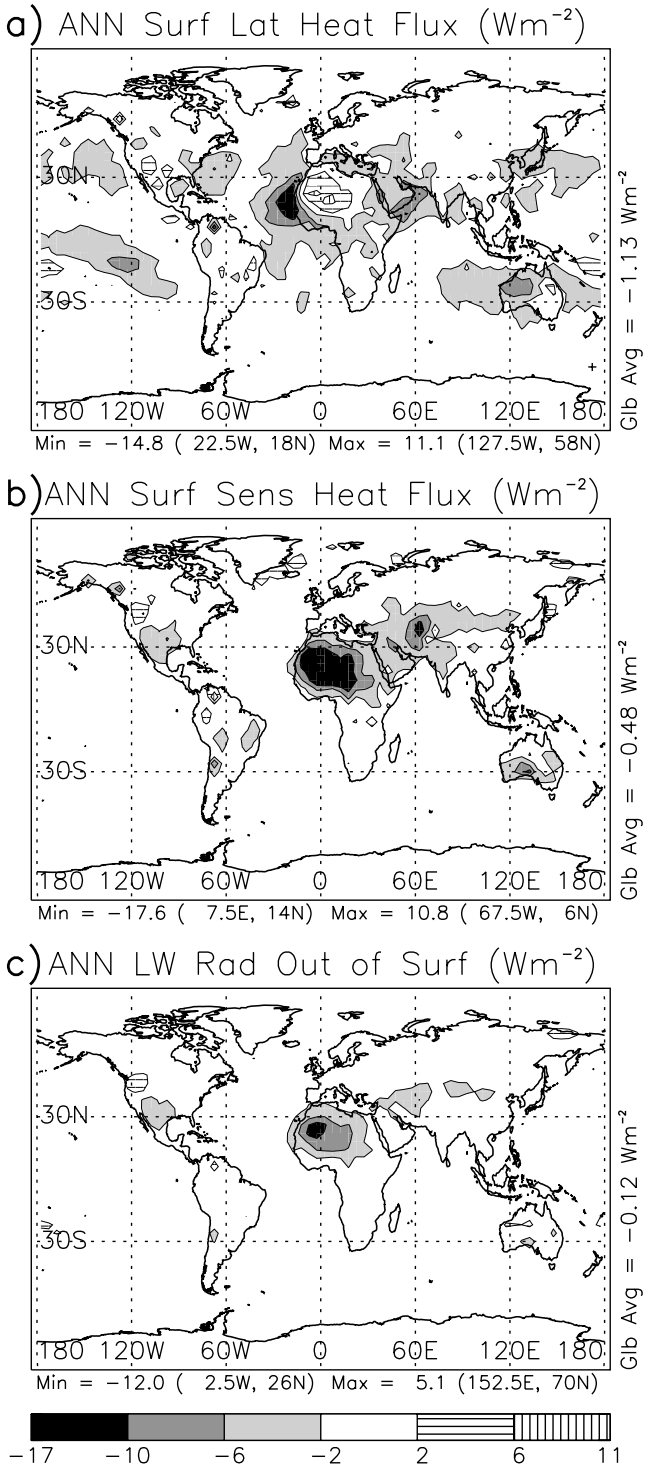

Figure 14. Annual average surface flux anomaly (W m^{-2}) in response to surface radiative forcing by dust particles. Anomalies are defined as the difference in surface flux between experiments with and without radiatively active dust. (a) Latent heat flux, (b) sensible heat flux, and (c) net upward longwave flux.

small longwave cooling in these regions (Figure 17a). This cooling is weak because of the small column water vapor, which allows efficient emission of longwave radiation by the surface directly to space, without absorption and re-emission within the intervening atmosphere. Given weak longwave cooling, a modest heating anomaly (5) can reverse the sign of the total diabatic heating within the column.

[45] Increasing evaporation over the Sahara with increasing particle absorption follows from the increasing precipitation in this region (Figure 16). To be sure, the occurrence of precipitation depends not only upon the local radiative forcing, but upon other contributions to the diabatic heating, which depend in a complicated way upon the anomalous circulation. For example, anomalous convergence of moisture determines the sign of δL $(P - E)$ in (5). Nonetheless, our simple argument suggests that dust radiative forcing is most likely to change the sign of the total diabatic heating over the desert, where the TOA forcing is large and positive, and the background longwave cooling is small.

[46] Our analysis of the anomalous surface energy balance neglects the radiative response at solar wavelengths: for example, by an increase in cloud cover that further reduces the incident sunlight. We measure the importance of this effect by comparing the surface radiative forcing to the net solar flux at the surface, as in Figure 18. A small difference indicates a negligible solar response. While comparison is complicated by internal variability of the model, the forcing and solar anomaly are almost identical beneath the dust layer. Over the Sahara, the solar anomaly is slightly more negative than the forcing, indicating an increase in cloud cover associated with the precipitation anomaly (Figure 19 shows low cloud cover; similar cloud cover anomalies are found at higher levels.) Over the Atlantic Ocean, the anomalous cloud cover is less spatially coherent and more difficult to interpret, although it generally increases with absorptivity downwind of the Sahara. As noted above, the rate of subsidence, which flushes lower levels with dry upper tropospheric air and thus inhibits cloud formation and precipitation, is smallest for the most absorbing particles. The increase in cloud cover with increasing aerosol absorption is counter to the "semidirect" effect described by *Hansen et al.* [1997b] in the same AGCM, where heating of aerosols within a cloud layer leads to a decrease in relative humidity and cloud cover. In that study, aerosol

Table 7. Global and Annual Average Surface Forcing and Surface Flux Anomalies (W m^{-2}) for AGCM Experiments with Reflecting Dust Particles ($1.1 \times \varpi$), Far-Travelled Saharan Particles ($1.0 \times \varpi$), and More Absorbing Particles ($0.9 \times \varpi$)

	$1.1 \times \varpi$	$1.0 \times \varpi$	$0.9 \times \varpi$
Surface Forcing	−1.01	−1.64	−2.54
Net Downward Solar	−0.84	−1.84	−3.35
Latent Heat	−1.30	−1.13	−1.04
Sensible Heat	0.03	−0.47	−1.22
Net Upward Longwave	0.57	−0.12	−1.05
	−0.70	−1.72	−3.31

Surface forcing is based upon the dust distribution calculated within each experiment. The forcing values for the more absorbing and reflecting experiments differ slightly from those in Table 3, which were calculated using the dust distribution from the far-travelled Saharan experiment ($1.0 \times \varpi$), but with varying optical properties.

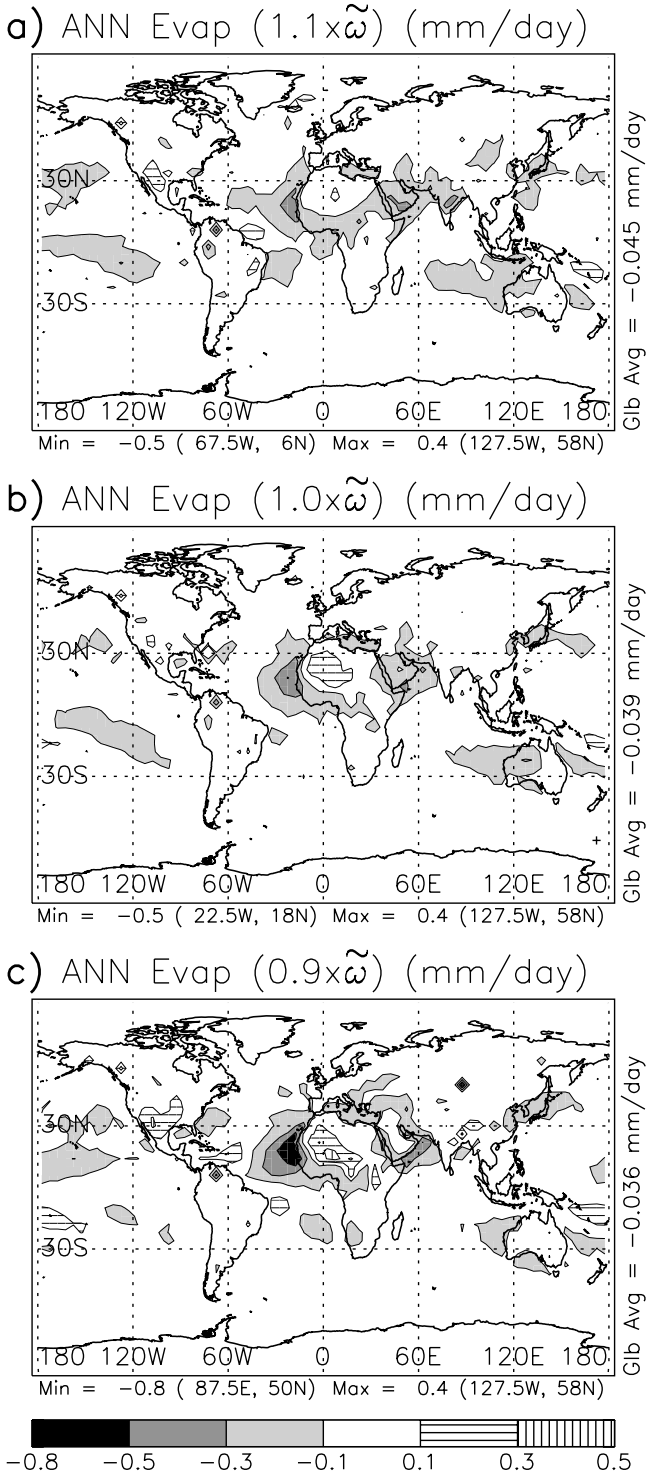

Figure 15. Anomalous evaporation (mm/day) for the experiment with (a) more reflecting particles (1.1 × $\tilde{\omega}$), (b) far-travelled Saharan dust (1.0 × $\tilde{\omega}$), and (c) more absorbing particles (0.9 × $\tilde{\omega}$).

heating was confined to a single model layer, rather than the deeper layer indicated in Figure 11, with a correspondingly smaller reduction of dry air subsiding into the boundary layer.

[47] There is an extensive literature linking rainfall over the Sahel to anomalous ocean temperatures in the tropical Atlantic. Wet years coincide with cold anomalies in the Gulf of Guinea [*Giannini et al.*, 2003], when the increased temperature contrast between the ocean and continent strengthens the African monsoon. Dust reduces sea surface temperature on the order of 0.5–1 K where the plume extends westward from the African coast [*Miller and Tegen*, 1998]. The cooling of the ocean surface by dust is an alternative mechanism for the AGCM increase in rainfall and evaporation over the Sahel. However, some studies argue that the anomalous SST pattern related to Sahelian rainfall includes warming in the Northern Hemisphere subtropics, beneath the dust plume [*Lamb and Peppler*, 1992]. An AGCM forced by the cold SST anomaly created by dust radiative forcing could be used to determine the anomaly's influence upon Sahelian rainfall.

[48] The AGCM demonstrates that while dust generally reduces evaporation and rainfall beneath the dust layer, these quantities may actually increase over dry regions, where dust is originally emitted. This represents a negative feedback to desertification, where dessication of the soil and subsequent dust emission cause an expansion of the rainy zone into the desert, inhibiting further emission. In our model, Saharan rainfall increases by 0.3 mm/day (Figure 16b), which corresponds to roughly 10 cm/year. This is merely 5% of the annual average rainfall within the ITCZ to the south (Figure 17b), but as large as the average at the northern edge of the Sahel. The rainfall increase would be larger if our model underestimates the actual dust load. Note that soil particles from the Sahel are enriched in hematite, a mineral which efficiently absorbs at solar wavelengths [*Sokolik and Toon*, 1999; *Claquin et al.*, 1999], which would increase the column warming and the precipitation anomaly (Figure 16c). The negative feedback to desertification opposes the reduction in rainfall by dust due to microphysical effects, where dust increases the number of available cloud condensation nuclei (CCN), reducing the average cloud droplet size. Rainfall is decreased as a consequence of the increased number of collisions required to form a raindrop [*Nicholson*, 2000; *Rosenfeld et al.*, 2001]. Modeling of this aerosol indirect effect by dust is currently restricted to case studies within a limited domain, and is not included in our AGCM.

[49] Despite the increase in desert rainfall by dust, the global effect of its surface forcing is to reduce rainfall. This in turn reduces wet deposition, as shown in Figure 20. This reduction is calculated by comparing the deposition rate between AGCM experiments with and without dust radiative forcing. Dust is a prognostic variable in both experiments, but alters the climate—and in turn is altered by these climate anomalies—only in the former. The global and annual mean wet deposition and wet deposition lifetimes are listed in Table 8. Dust radiative forcing increases the wet deposition lifetime from 12.5 to 12.8 days, compared to the experiment where dust is present but has no radiative effect—with an additional increase of over a full day to 13.9 for more absorbing particles. While dust may increase rainfall and inhibit emission over deserts, its global effect is to increase the dust load; it represents a local negative feedback to

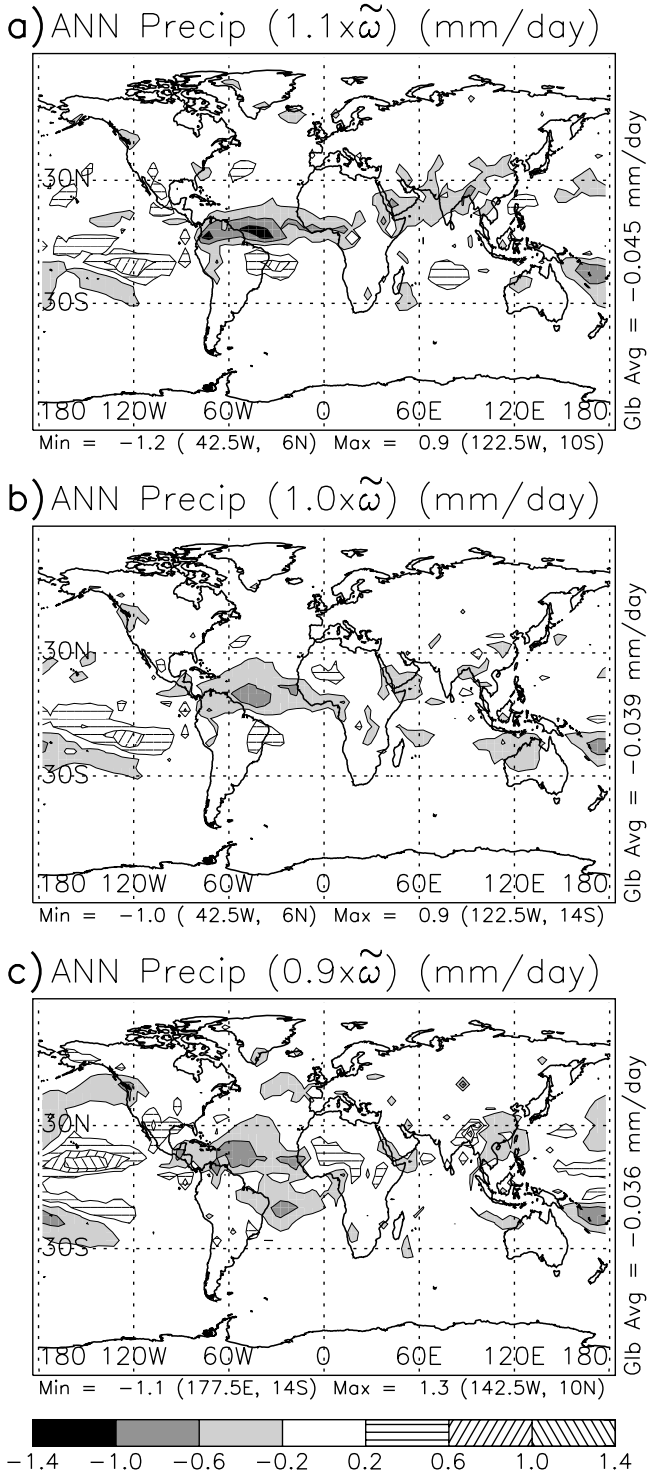

Figure 16. Same as Figure 15 but for anomalous precipitation (mm/day).

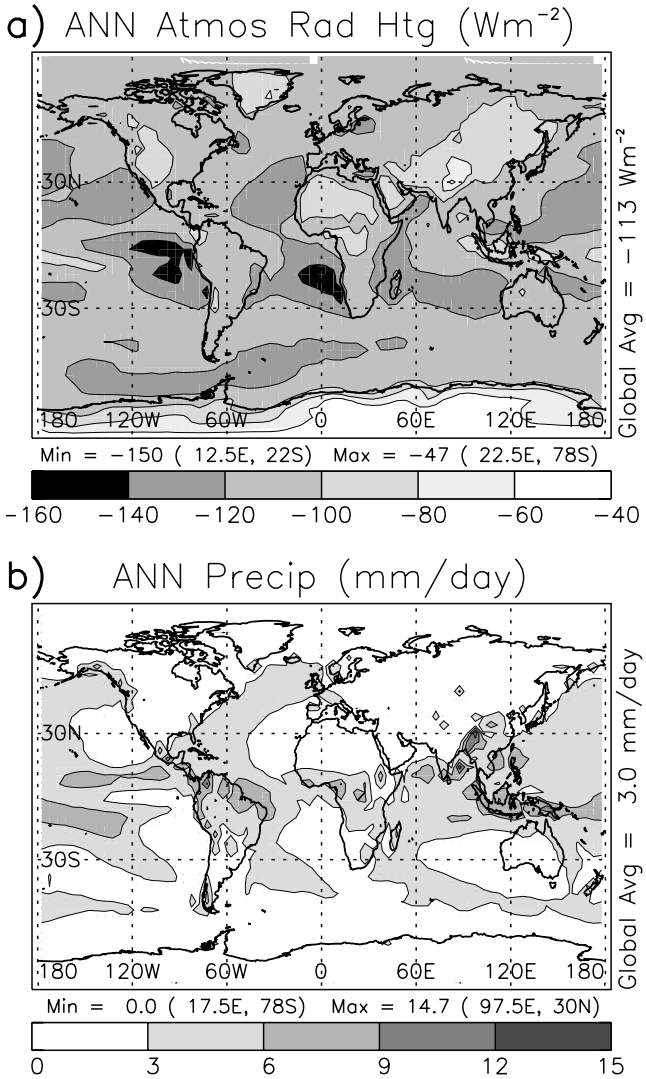

Figure 17. (a) Atmospheric radiative heating (W m^{-2}) and (b) precipitation (mm/day), in the absence of dust radiative forcing.

desertification but a positive feedback to the global dust burden.

[50] In the current climate, this positive feedback is modest. For the emission and dry deposition calculated by the AGCM, the dust load is increased by only 1.0% due to the lengthened wet deposition lifetime. This is comparable to the 1.3% reduction of global evaporation and precipitation, based upon the −1.13 W m^{-2} global anomaly of the surface latent heat flux (Table 7). Nonetheless, the actual percentages could be between two and three times larger if the present-day dust burden is as large as estimated by *Ginoux et al.* [2001].

[51] The reduction in evaporation and lengthening of the wet deposition lifetime by dust radiative forcing were greater during the Last Glacial Maximum (LGM), when dust deposition increased substantially in deep sea sediments [*Rea*, 1994] and high latitude ice cores [*Petit et al.*, 1990; *Biscaye et al.*, 1997; *Reader et al.*, 1999; *Mahowald et al.*, 1999; *Kohfeld and Harrison*, 2001]. Estimates of the LGM dust burden range from one-and-a-half [*Lunt and Valdes*, 2002] to two-and-a-half [*Mahowald et al.*, 1999] to three [*Werner et al.*, 2002] times the present-day value. If we assume our present-day burden is an underestimate by a factor of two, and that the LGM burden is two times greater, then assuming a corresponding increase in surface radiative forcing, the reduction in evaporation and precipitation due to the radiative effect of dust alone is just over 5%. *Yung et al.* [1996] hypothesize that the glacial dust load was larger due to a reduction in rainfall by the cooler climate leading to a decrease in wet deposition. *Bush and Philander* [1999] calculate this rainfall reduction to be 11%, so that the additional reduction due to dust could be a significant source of aerosol. Decreased precipitation by dust can also reduce vegetation, and increase potential source areas for emission, another positive feedback to the dust load. *Mahowald et al.* [1999] show that the decrease in vegetation by the reduction in temperature, precipitation, and atmospheric CO_2 during the LGM result in substantially greater emission of dust.

[52] Extrapolation of the current forcing to LGM values is highly uncertain [*Harrison et al.*, 2001], due to the greater fraction of the LGM dust load at high latitudes, where there are large changes in surface albedo due to the extensive continental ice sheets and reduced vegetation. Both of these effects would combine to make the surface brighter, which would increase the surface forcing and the associated reduction in evaporation and precipitation beyond that of our estimate. Despite this caveat, our extrapolation suggests that the reduction of the LGM hydrologic cycle by dust radiative forcing is large enough—compared to the reduction due solely to the cooler climate—to justify its explicit calculation with an AGCM.

5. Conclusions

[53] Although its importance to climate has long been recognized [*Coakley and Cess*, 1985], radiative forcing by dust aerosols remains highly uncertain. While aerosol forcing is typically characterized by its TOA value [*Intergovernmental Panel on Climate Change*, 2001], the surface forcing is also fundamental to the climate response, especially for absorbing aerosols like dust, where forcing at the two levels may be quite different. This difference represents radiative heating displaced from the surface into the dust layer [*Miller and Tegen*, 1999; *Ramanathan et al.*, 2001].

[54] Using a global dust distribution derived by the NASA GISS AGCM, we estimate the surface forcing and atmospheric radiative heating, emphasizing their sensitivity to aspects of the dust distribution that vary widely among models, and are poorly constrained by observations. Global surface forcing is negative due to absorption and reflection of incident solar radiation within the overlying dust layer, where radiative heating offsets the tropic-wide longwave cooling. While the dust mixing ratio is largest near the surface, radiative heating remains substantial throughout the troposphere. This is important to the climate response, which is largest when the

radiative forcing is separated from the boundary layer [*Miller and Tegen*, 1999]. In this case, dust heating is balanced in the tropics by reduced adiabatic subsidence, or by reduced eddy heat convergence in midlatitudes, which leads to an adjustment to surface air temperature. In contrast, radiative heating within the boundary layer is compensated mainly by a change in the surface sensible heat flux via the ground temperature, which allows the air temperature to remain relatively unperturbed.

[55] Our forcing estimate is most sensitive to the current uncertainty in aerosol burden. The global burden computed by the AGCM is just under 15 Tg. This is at the low end of recent model estimates that can exceed ours by more than a factor of two, while remaining consistent with observed values of column amount and surface concentration [*Ginoux et al.*, 2001; *Tegen et al.*, 2002; *Luo et al.*, 2003; *Zender et al.*, 2003a]. Because the global forcing is nearly linear within this range, the actual forcing and atmospheric radiative heating are possibly over a factor of two greater than our model estimate. Observational estimates of the aerosol burden have a similar uncertainty: satellite inferences of the total aerosol optical thickness vary by a factor of two over the oceans [*Myhre et al.*, 2004]. The particle size distribution also varies greatly among models. The ratio of silt particles to clay varies by fourfold, although the surface forcing and atmospheric radiative heating vary only by 10% over this range.

[56] Dust radiative forcing is calculated by assuming particle optical properties that are globally uniform, taken from laboratory measurements of far-traveled Saharan dust [*Volz*, 1973; *Patterson et al.*, 1977]. Solar absorption by Saharan dust remains under debate. The absorption inferred from Sun photometers is substantially smaller [*Kaufman et al.*, 2001; *Sinyuk et al.*, 2003]. In contrast, *Weaver et al.* [2002] find that our adopted optical properties lead to the best agreement of dust radiative forcing with satellite measurements. In addition to the uncertainty of measured absorption, the actual forcing will depart from our calculated value due to geographic variations in the mineralogy of source regions, along with the presence of water and sulfates on the aerosol surface. We calculate that a 10% increase in the particle single scatter albedo (corresponding to reduced absorption) halves the surface forcing, and reduces the associated column heating to nearly zero. This change bounds the reduction in solar absorption proposed for Saharan dust by the in situ measurements of *Sinyuk et al.* [2003]. Conversely, a 10% decrease in particle absorption nearly doubles the surface forcing and atmospheric radiative heating.

[57] Regional variations in mineralogical composition of soil particles are fundamental to the forcing and regional climate response, along with the associated anthropogenic "fingerprint" of soil dust that must be distinguished from that due to greenhouse gases. We are currently introducing distinct aerosol mineralogies using recent data sets by *Claquin et al.* [1999], describing the regional distribution of various mineral types, and *Sokolik and Toon* [1999], who tabulate wavelength-dependent indices of refraction for these minerals. Biogeochemical processes are sensitive to the precise mineral content of the deposited aerosol. Deposition of iron-rich minerals, such as hematite, fertilize the

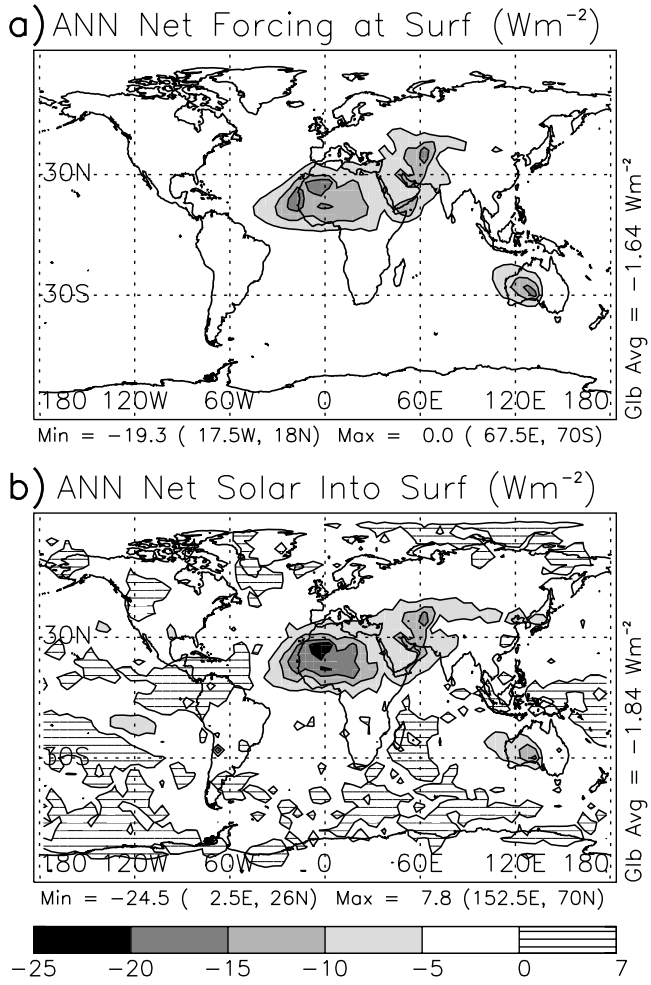

Figure 18. Annual average (a) surface radiative forcing by dust and (b) anomalous net solar flux into the surface, both in W m^{-2}.

ocean mixed layer, increasing the productivity of marine ecosystems and the ocean uptake of CO_2 [*Martin*, 1991; *Bishop et al.*, 2002]. By this mechanism, dust is hypothesized to have modulated the atmospheric CO_2 concentration during the last glacial cycle [*Archer et al.*, 2000; *Broecker*, 2000; *Ridgwell*, 2003]. Certain minerals also supply crucial nutrients to soils far downwind of the source region [*Swap et al.*, 1992; *Chadwick et al.*, 1999].

[58] Through radiative forcing at the surface, dust alters the hydrologic cycle. The reduction in sunlight beneath the dust layer is balanced globally by diminished evaporation, with a secondary reduction in the surface sensible heat flux [*Coakley and Cess*, 1985]. Despite its global reduction, we find that evaporation is increased along with rainfall by dust over the Sahara. We suggest three reasons for this contrasting regional response. First, radiative heating of the atmosphere by dust, which opposes longwave cooling and subsidence, is large over the bright desert surface (c.f. equation (5)). Second, the dust load and radiative forcing are large over arid regions, where the absence of soil moisture leaves particles susceptible to wind erosion. Finally, radiative cooling is smallest over

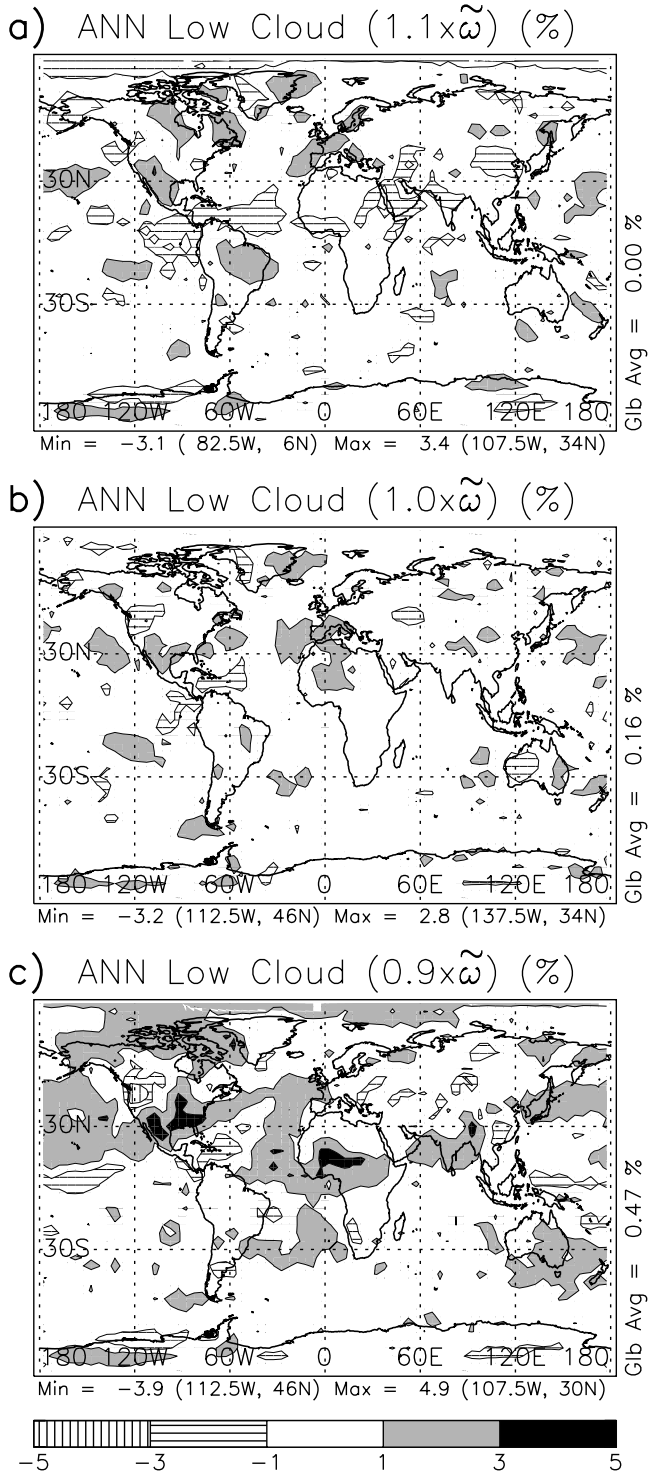

Figure 19. Same as Figure 15 but for anomalous low cloud cover (percent).

deserts, where the column moisture is small, and the surface efficiently emits longwave radiation directly to space. Over the Sahara, then, a modest heating anomaly by dust radiative forcing can change the sign of the total diabatic heating, resulting in ascent and precipitation. This represents a negative feedback to dust emission resulting from desertification. The strength of this feedback depends upon the column radiative heating by dust, which increases with particle absorption. This accounts for the reduction in magnitude of the global evaporative anomaly as particle absorption is increased, despite the increase in the magnitude of surface forcing. The local negative feedback opposes the decrease in rainfall due to the aerosol indirect effect upon cloud microphysics [*Nicholson*, 2000; *Rosenfeld et al.*, 2001]. Quantifying the relative importance of these two feedbacks will require more precise measurements of particle absorption, along with a better understanding of the interaction between dust and cloud microphysics on a global scale.

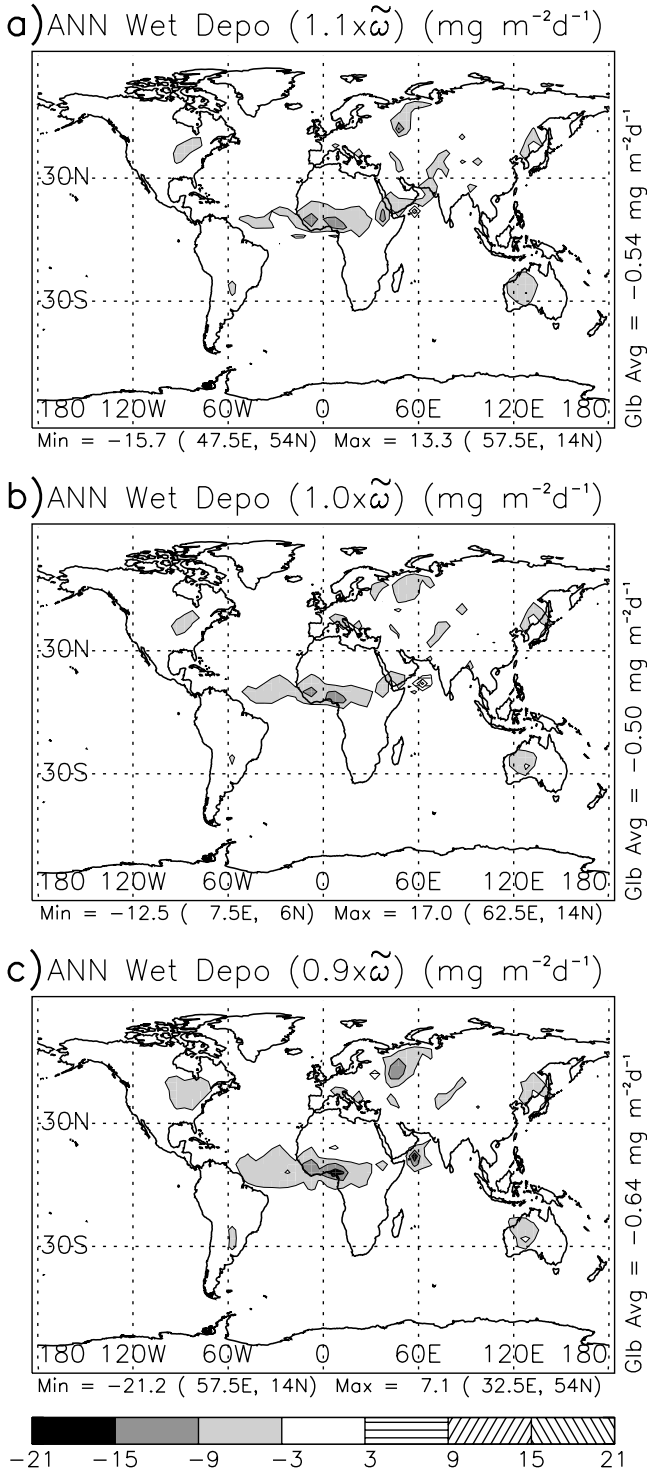

Figure 20. Same as Figure 15 but for anomalous wet deposition (mg m^{-2} day^{-1}).

Table 8. Global and Annual Wet Deposition (mg m^{-2} d^{-1}), Load (mg m^{-2}), and Wet Deposition Lifetime (d) for AGCM Experiments With Radiatively Passive Dust, More Reflecting Dust Particles (1.1 × ϖ), Far-Travelled Saharan Particles (1.0 × ϖ), and More Absorbing Particles (0.9 × ϖ)

	Wet Deposition (mg m^{-2} d^{-1})	Load (mg m^{-2})	Wet Lifetime (d)
Passive dust	2.75	34.3	12.5
1.1 × ϖ	2.21	27.6	12.5
1.0 × ϖ	2.24	28.6	12.8
0.9 × ϖ	2.10	29.2	13.9

The passive dust experiment calculates the trajectory of dust aerosols, but omits the particles' radiative effect.

[59] Despite the increase in desert precipitation, the global reduction of rainfall by dust reduces the wet deposition efficiency. Thus while radiative forcing by dust creates a local negative feedback to desertification, it increases the aerosol burden globally. For the current climate, this effect is modest, as dust reduces precipitation by only a percent or two. The associated wet deposition lifetime increases from 12.5 to 12.8 days, although this lifetime is as long as 13.9 days if the particle absorption is increased by 10%. However, for glacial climates, when the inferred load is substantially larger [*Kohfeld and Harrison*, 2001], we estimate that the reduction in precipitation could exceed 5%, roughly half of the precipitation decrease resulting simply from the colder climate [*Bush and Philander*, 1999]. This suggests that dust radiative forcing contributes non-negligibly to the reduction of the hydrologic cycle during glacial climates. In addition to its effect upon the aerosol lifetime, the reduction in rainfall has the potential to reduce vegetation, expanding potential regions of dust emission. *Mahowald et al.* [1999] show that the contraction of vegetated areas by the colder and drier LGM climate contributes substantially to the greater mobilization of dust. The ability of dust to reduce vegetative cover is a potentially large positive feedback, given that the reduction of rainfall by dust is roughly half that due to all other processes. Our estimated radiative forcing by dust for a glacial climate, based upon extrapolation from the present, is highly uncertain, due to the substantial differences in the geographic distribution of dust as well as the surface albedo between the two climates [*Kohfeld and Harrison*, 2001]. However, the reflective continental ice sheets and diminished forest area might actually increase the surface forcing beyond that suggested by our estimate. Despite its uncertainty, our estimated reduction in the hydrologic cycle by dust during glacial times is large enough to suggest that its explicit calculation is worthwhile.

[60] **Acknowledgments.** This article was greatly improved by the comments of the anonymous reviewers. We thank Reto Ruedy for guidance with the radiative forcing calculations, along with Brian Cairns and Andy Lacis for their expertise regarding aerosol radiative effects. We are grateful to Reha Cakmur for advice about the sensitivity of the model dust distribution. This work was supported by the Climate Dynamics Program of the National Science Foundation through ATM-97-27872.

References

Andreae, M. (1995), Climatic effects of changing atmospheric aerosol levels, in *Future Climates of the World: A Modelling Perspective, World Survey of Climatology*, vol. 16, edited by A. Henderson-Sellers, pp. 347–398, Elsevier Sci., New York.

Archer, D., A. Winguth, D. Lea, and N. Mahowald (2000), What caused the glacial/interglacial atmospheric pCO_2 cycles?, *Rev. Geophys.*, *38*, 159–189.

Arya, S. P. (1988), *Introduction to Micrometeorology*, 307 pp., Academic, San Diego, Calif.

Biscaye, P. E., F. E. Grousset, M. Revel, S. van der Gaast, G. A. Zielinski, A. Vaars, and G. Kukla (1997), Asian provenance of glacial dust (stage 2) in the Greenland Ice Sheet Project 2 ice core, Summit, Greenland, *J. Geophys. Res.*, *102*, 26,765–26,781.

Bishop, J. K. B., R. E. Davis, and J. T. Sherman (2002), Robotic observations on dust storm enhancement of carbon biomass in the North Pacific, *Science*, *298*, 817–821.

Bory, A. J.-M., P. E. Biscaye, A. Svensson, and F. E. Grousset (2002), Seasonal variability in the origin of recent atmospheric mineral dust at NorthGRIP, Greenland, *Earth Planet. Sci. Lett.*, *196*, 123–134.

Bory, A. J.-M., P. E. Biscaye, and F. E. Grousset (2003), Two distinct seasonal Asian source regions for mineral dust deposited in Greenland (NorthGRIP), *Geophys. Res. Lett.*, *30*(4), 1167, doi:10.1029/2002GL016446.

Broecker, W. S. (2000), Abrupt climate change: Causal constraints provided by the paleoclimate record, *Earth-Sci. Rev.*, *51*, 137–154.

Bush, A. B. G., and S. G. H. Philander (1999), The climate of the Last Glacial Maximum: Results from a coupled atmosphere-ocean general circulation model, *J. Geophys. Res.*, *104*, 24,509–24,525.

Carlson, T. N., and J. M. Prospero (1972), The large-scale movement of Saharan air outbreaks over the northern equatorial Atlantic, *J. Appl. Meterol.*, *11*, 283–297.

Cess, R., et al. (1995), Absorption of solar radiation by clouds: Observations versus models, *Science*, *267*, 496–499.

Chadwick, O. A., L. A. Derry, P. M. Vitousek, B. J. Huebert, and L. O. Hedin (1999), Changing sources of nutrients during four million years of ecosystem development, *Nature*, *397*, 491–497.

Chester, R., and L. R. Johnson (1971), Trace element geochemistry of North Atlantic aeolian dusts, *Nature*, *231*, 176–178.

Chiapello, I. G., C. B. Bergametti, F. Dulac, I. Jankowiak, C. Liousse, and E. Soares (1999), Contribution of the different aerosol species to the aerosol mass load and optical depth over the Northeastern Tropical Atlantic, *J. Geophys. Res.*, *104*, 4025–4035.

Claquin, T., M. Schulz, Y. Balkanski, and O. Boucher (1998), Uncertainties in assessing radiative forcing by mineral dust, *Tellus, Ser B.*, *50*, 491–505.

Claquin, T., M. Schulz, and Y. Balkanski (1999), Modeling the mineralogy of atmospheric dust sources, *J. Geophys. Res.*, *104*, 22,243–22,256.

Coakley, J. A., and R. D. Cess (1985), Response of the NCAR Community Climate Model to the radiative forcing by the naturally occurring tropospheric aerosol, *J. Atmos. Sci.*, *42*, 1677–1692.

d'Almeida, G. A. (1986), A model for Saharan dust transport, *J. Clim. Appl. Meteorol.*, *25*, 903–916.

Dentener, F. J., G. R. Carmichael, Y. Zhang, J. Lelieveld, and P. J. Crutzen (1996), Role of mineral aerosol as a reactive surface in the global troposphere, *J. Geophys. Res.*, *101*, 22,869–22,889.

Duce, R. A. (1995), Sources, distributions, and fluxes of mineral aerosols and their relation to climate, in *Aerosol Forcing of Climate*, edited by R. J. Charlson and J. Heintzenberg, pp. 43–72, John Wiley, Hoboken, N. J.

Duce, R. A., C. K. Unni, B. J. Ray, J. M. Prospero, and J. T. Merrill (1980), Long-range atmospheric transport of soil dust from Asia to the Tropical North Pacific: Temporal variability, *Science*, *209*, 1522–1524.

Duce, R. A., et al. (1991), The atmospheric input of trace species to the world ocean, *Global Biogeochem. Cycles*, *5*, 193–259.

Dufresne, J.-L., C. Gautier, and Y. Fouquart (2002), Longwave scattering effects of mineral aerosols, *J. Atmos. Sci.*, *59*, 1959–1966.

Galperin, B., L. H. Kantha, S. Hassid, and A. Rosatti (1988), A quasi-equilibrium turbulent energy model for geophysical flows, *J. Atmos. Sci.*, *45*, 55–62.

Giannini, A., R. Saravanan, and P. Chang (2003), Oceanic forcing of Sahel rainfall on interannual to interdecadal time scales, *Nature*, *302*, 1027–1030.

Gillette, D. (1978), A wind tunnel simulation of the erosion of soil: Effect of soil texture, sandblasting, wind speed, and soil consolidation on dust production, *Atmos. Environ.*, *12*, 1735–1743.

Ginoux, P. (2003), Effects of nonsphericity on mineral dust modeling, *J. Geophys. Res.*, *108*, 4052–4061, doi:10.1029/2002JD002516.

Ginoux, P., M. Chin, I. Tegen, J. Prospero, B. Holben, O. Dubovik, and S. J. Lin (2001), Sources and distributions of aerosols simulated with the GOCART model, *J. Geophys. Res.*, *106*, 20,255–20,273.

Goudie, A. S., and N. J. Middleton (2001), Saharan dust storms: Nature and consequences, *Earth-Sci. Rev.*, *56*, 179–204.

Grousset, F. E., P. Ginoux, A. Bory, and P. E. Biscaye (2003), Case study of a Chinese dust plume reaching the French Alps, *Geophys. Res. Lett.*, *30*(6), 1277, doi:10.1029/2002GL016833.

Guelle, W., Y. Balkanski, M. Schulz, B. Marticorena, G. Bergametti, C. Moulin, R. Arimoto, and K. Perry (2000), Modeling the atmospheric distribution of mineral aerosol: Comparison with ground measurements and satellite observations for yearly and synoptic timescales over the North Atlantic, *J. Geophys. Res.*, *105*, 1997–2012.

Hansen, J., M. Sato, and R. Ruedy (1997a), Radiative forcing and climate response, *J. Geophys. Res.*, *102*, 6831–6864.

Hansen, J., et al. (1997b), Forcings and chaos in interannual to decadal climate change, *J. Geophys. Res.*, *102*, 25,679–25,720.

Harrison, S. P., K. E. Kohfeld, C. Roelandt, and T. Claquin (2001), The role of dust in climate changes today, at the last glacial maximum and in the future, *Earth Sci. Rev.*, *54*, 43–80.

Hartke, G., and D. Rind (1997), Improved surface and boundary layer models for the Goddard Institute for Space Studies general circulation model, *J. Geophys. Res.*, *102*, 16,407–16,422.

Haywood, J., and O. Boucher (2000), Estimates of the direct and indirect radiative forcing due to tropospheric aerosols: A review, *Rev. Geophys.*, *38*, 513–543.

Herman, J. R., P. K. Bhartia, O. Torres, C. Hsu, C. Seftor, and E. Celarier (1997), Global distribution of UV-absorbing aerosols from Nimbus-7/TOMS data, *J. Geophys. Res.*, *102*, 16,911–16,922.

Holben, B. N., et al. (1998), AERONET: A federated instrument network and data archive for aerosol characterization, *Remote Sens. Environ.*, *66*, 1–16.

Holton, J. R. (1992), *An introduction to dynamic meteorology*, 511 pp., Academic, San Diego, Calif.

Husar, R. B., J. M. Prospero, and L. L. Stowe (1997), Characterization of tropospheric aerosols over the oceans with the NOAA advanced very high resolution radiometer optical thickness operational product, *J. Geophys. Res.*, *102*, 16,889–16,909.

Intergovernmental Panel on Climate Change (2001), *Summary for Policymakers: A Report of Working Group I*, edited by J. T. Houghton et al., 881 pp., Cambridge Univ. Press, New York.

Karyampudi, V., et al. (1999), Validation of the Saharan dust plume conceptual model using lidar, Meteostat, and ECMWF data, *Bull. Am. Meteorol. Soc.*, *80*, 1045–1075.

Kaufman, Y. J., D. Tanré, O. Dubovik, A. Karnieli, and L. A. Remer (2001), Absorption of sunlight by dust as inferred from satellite and ground-based remote sensing, *Geophys. Res. Lett.*, *28*, 1479–1482.

King, M., Y. Kaufman, D. Tanre, and T. Nakajima (1999), Remote sensing of tropospheric aerosols from space: Past, present, and future, *Bull. Am. Meteorol. Soc.*, *11*, 2229–2259.

Kohfeld, K., and S. P. Harrison (2001), DIRTMAP: The geologic record of dust, *Earth-Sci. Rev.*, *54*, 81–114.

Lacis, A. A., and M. I. Mishchenko (1995), Climate forcing, climate sensitivity, and climate response: A radiative modeling perspective on atmospheric aerosols, in *Aerosol Forcing of Climate*, edited by R. J. Charlson and J. Heintzenberg, chap. 2, pp. 11–42, John Wiley, Hoboken, N. J.

Lamb, P. J., and R. A. Peppler (1992), Further case studies of tropical Atlantic surface atmospheric and oceanic patterns associated with sub-Saharan drought, *J. Clim.*, *5*, 476–488.

Lau, K.-M., J. H. Kim, and Y. Sud (1996), Intercomparison of hydrologic processes in AMIP GCMs, *Bull. Am. Meteorol. Soc.*, *77*, 2209–2227.

Li, X., H. Maring, D. Savoie, K. Voss, and J. M. Prospero (1996), Dominance of mineral dust in aerosol light-scattering in the North Atlantic trade winds, *Nature*, *380*, 416–419.

Liao, H., and J. H. Seinfeld (1998), Radiative forcing by mineral dust aerosols: Sensitivity to key variables, *J. Geophys. Res.*, *103*, 31,637–31,645.

Lunt, D. J., and P. J. Valdes (2002), Dust deposition and provenence at the Last Glacial Maximum and present day, *Geophys. Res. Lett.*, *29*(22), 2085, doi:10.1029/2002GL015656.

Luo, C., N. M. Mahowald, and J. del Corral (2003), Sensitivity study of meteorological parameters on mineral aerosol mobilization, transport, and distribution, *J. Geophys. Res.*, *108*(D15), 4447, doi:10.1029/2003JD003483.

Mahowald, N., and C. Luo (2003), A less dusty future?, *Geophys. Res. Lett.*, *30*(17), 1903, doi:10.1029/2003GL017880.
Mahowald, N., K. Kohfeld, M. Hansson, Y. Balkanski, S. P. Harrison, I. C. Prentice, M. Schulz, and H. Rodhe (1999), Dust sources and deposition during the last glacial maximum and current climate: A comparison of model results with paleodata from ice cores and marine sediments, *J. Geophys. Res.*, *104*, 15,895–15,916.
Mahowald, N., C. Zender, C. Luo, D. Savoie, O. Torres, and J. del Corral (2002), Understanding the 30-year Barbados desert dust record, *J. Geophys. Res.*, *107*(D21), 4561, doi:10.1029/2002JD002097.
Marticorena, B., G. Bergametti, and M. Legrand (1999), Comparison of emission models used for large-scale simulation of the mineral dust cycle, *Contrib. Atmos. Phys.*, *72*, 151–160.
Martin, J. H. (1991), Iron still comes from above, *Nature*, *353*, 123.
Matthews, E. (1983), Global vegetation and land use: New high-resolution data bases for climate studies, *J. Clim. Appl. Meteorol.*, *22*, 474–487.
Mellor, G. L., and T. Yamada (1982), Development of a turbulent closure model for geophysical fluid problems, *Rev. Geophys. and Space Phys.*, *20*, 851–875.
Menon, S., J. Hansen, L. Nazarenko, and Y. Luo (2002), Climate effects of black carbon aerosols in China and India, *Science*, *297*, 2250–2253.
Meywerk, J., and V. Ramanathan (1999), Observations of the spectral clear-sky aerosol forcing over the Tropical Indian Ocean, *J. Geophys. Res.*, *104*, 24,359–24,370.
Miller, J. R., G. L. Russell, and L.-C. Tsang (1983), Annual oceanic heat transports computed from an atmospheric model, *Dyn. Atmos. Oceans*, *7*, 95–109.
Miller, R. L., and I. Tegen (1998), Climate response to soil dust aerosols, *J. Clim.*, *11*, 3247–3267.
Miller, R. L., and I. Tegen (1999), Radiative forcing of a tropical direct circulation by soil dust aerosols, *J. Atmos. Sci.*, *56*, 2403–2433.
Moulin, C., F. Guillard, F. Dulac, and C. E. Lambert (1997), Long-term daily monitoring of Saharan dust load over ocean using Meteosat ISCCP-B2 data: 1. Methodology and preliminary results for 1983–1994 in the Mediterranean, *J. Geophys. Res.*, *102*, 16,947–16,958.
Myhre, G., and F. Stordal (2001), Global sensitivity experiments of the radiative forcing due to mineral aerosols, *J. Geophys. Res.*, *106*, 18,193–18,204.
Myhre, G. A., et al. (2004), Intercomparison of satellite retrieved aerosol optical depth over ocean, *J. Atmos. Sci.*, in press.
Nicholson, S. (2000), Land surface processes and Sahel climate, *Rev. Geophys.*, *38*, 117–139.
N'Tchayi Mbourou, G., J. Bertrand, and S. Nicholson (1997), The diurnal and seasonal cycles of wind-borne dust over Africa North of the Equator, *J. Appl. Meterol.*, *36*, 868–882.
Parrington, J. R., W. H. Zoller, and N. K. Aras (1983), Asian dust: Seasonal transport to the Hawaiian Islands, *Science*, *220*, 195–197.
Patterson, E. M., D. A. Gillette, and B. H. Stockton (1977), Complex index of refraction between 300 and 700 nm for Saharan aerosols, *J. Geophys. Res.*, *82*, 3153–3160.
Perlwitz, J., I. Tegen, and R. L. Miller (2001), Interactive soil dust aerosol model in the GISS GCM. Part I: Sensitivity of the soil dust cycle to radiative properties of soil dust aerosols, *J. Geophys. Res.*, *106*, 18,167–18,192.
Perry, K. D., T. A. Cahill, R. A. Eldred, D. D. Dutcher, and T. E. Gill (1997), Long-range transport of North African dust to the eastern United States, *J. Geophys. Res.*, *102*, 11,225–11,238.
Petit, J. R., L. Mournier, J. Jouzel, Y. S. Korotkevich, V. I. Kotlyakov, and C. Lorius (1990), Paleoclimatological and chronological implications of the Vostok core dust record, *Nature*, *343*, 56–58.
Pierrehumbert, R. T. (1995), Thermostats, radiator fins, and the runaway greenhouse, *J. Atmos. Sci.*, *52*, 1784–1806.
Prather, M. (1986), Numerical advection by conservation of second-order moments, *J. Geophys. Res.*, *91*, 6671–6680.
Prospero, J. (1996), The atmospheric transport of particles to the ocean, in *Particle Flux in the Ocean*, edited by V. Ittekkot et al., chap. 3, pp. 19–56, J. Wiley, Hoboken, N. J.
Prospero, J. M. (1999), Long-term measurements of the transport of African mineral dust to the southeastern United States: Implications for regional air quality, *J. Geophys. Res.*, *104*, 15,917–15,927.
Prospero, J. M., and R. T. Nees (1977), Dust concentration in the atmosphere of the equatorial North Atlantic: Possible relationship to the Sahelian drought, *Science*, *196*, 1196–1198.
Prospero, J. M., R. A. Glaccum, and R. T. Nees (1981), Atmospheric transport of soil dust from Africa to South America, *Nature*, *289*, 570–572.
Prospero, J. M., P. Ginoux, O. Torres, and S. Nicholson (2002), Environmental characterization of global sources of atmospheric soil dust derived from NIMBUS-7 TOMS absorbing aerosol product, *Rev. Geophys.*, *40*(1), 1002, doi:10.1029/2000RG000095.
Ramanathan, V., P. J. Crutzen, J. T. Kiehl, and D. Rosenfeld (2001), Aerosols, climate, and the hydrologic cycle, *Science*, *294*, 2119–2124.
Rea, D. K. (1994), The paleoclimatic record provided by eolian deposition in the deep sea: The geologic history of wind, *Rev. Geophys.*, *32*, 159–195.
Reader, M. C., I. Fung, and N. McFarlane (1999), The mineral dust aerosol cycle during the Last Glacial Maximum, *J. Geophys. Res.*, *104*, 9381–9398.
Ridgwell, A. J. (2003), Implications of the glacial CO_2 "iron hypothesis" for Quaternary climate change, *Geochem. Geophys. Geosyst.*, *4*(9), 1076, doi:10.1029/2003GC000563.
Rosenfeld, D., Y. Rudich, and R. Lahav (2001), Desert dust suppressing precipitation: A possible desertification feedback loop, *Proc. Natl. Acad. Sci. U.S.A.*, *98*, 5975–5980.
Schulz, M., Y. Balkanski, W. Guelle, and F. Dulac (1998), Treatment of aerosol size distribution in a global transport model: Validation with satellite-derived observations for a Saharan dust episode, *J. Geophys. Res.*, *103*, 10,579–10,592.
Shao, Y., M. R. Raupach, and P. A. Findlater (1993), Effect of saltation bombardment on the entrainment of dust by wind, *J. Geophys. Res.*, *98*, 12,719–12,726.
Sinyuk, A., O. Torres, and O. Dubovik (2003), Combined use of satellite and surface observations to infer the imaginary part of the refractive index of Saharan dust, *Geophys. Res. Lett.*, *30*(2), 1081, doi:10.1029/2002GL016189.
Sokolik, I., and G. Golitsyn (1993), Investigation of optical and radiative properties of atmospheric dust particles, *Atmos. Environ., Part A*, *27*, 2509–2517.
Sokolik, I. N., and O. Toon (1996), Direct radiative forcing by anthropogenic airborne mineral aerosols, *Nature*, *381*, 681–683.
Sokolik, I. N., and O. B. Toon (1999), Incorporation of mineralogical composition into models of the radiative properties of mineral aerosol from UV to IR wavelengths, *J. Geophys. Res.*, *104*, 9423–9444.
Sokolik, I., A. Andronova, and T. C. Johnson (1993), Complex refractive index of atmospheric dust aerosols, *Atmos. Environ., Part A*, *27*, 2495–2502.
Swap, R., M. Garstang, S. Greco, R. Talbot, and P. Kållberg (1992), Saharan dust in the Amazon basin, *Tellus, Ser. B*, *44*, 133–149.
Tegen, I., and I. Fung (1994), Modeling of mineral dust in the atmosphere: Sources, transport, and optical thickness, *J. Geophys. Res.*, *99*, 22,897–22,914.
Tegen, I., and I. Fung (1995), Contribution to the atmospheric mineral aerosol load from land surface modification, *J. Geophys. Res.*, *100*, 18,707–18,726.
Tegen, I., and A. A. Lacis (1996), Modeling of particle influence on the radiative properties of mineral dust aerosol, *J. Geophys. Res.*, *101*, 19,237–19,244.
Tegen, I., and R. Miller (1998), A general circulation model study on the interannual variability of soil dust aerosol, *J. Geophys. Res.*, *103*, 25,975–25,995.
Tegen, I., A. A. Lacis, and I. Fung (1996), The influence on climate forcing of mineral aerosols from disturbed soils, *Nature*, *380*, 419–422.
Tegen, I., P. Hollrig, M. Chin, I. Fung, D. Jacob, and J. Penner (1997), Contribution of different aerosol species to the global aerosol extinction optical thickness: Estimates from model results, *J. Geophys. Res.*, *102*, 23,895–23,915.
Tegen, I., S. P. Harrison, K. Kohfeld, I. C. Prentice, and M. Heimann (2002), The impact of vegetation and preferential source areas on global dust aerosol: Results from a model study, *J. Geophys. Res.*, *107*(D21), 4576, doi:10.1029/2001JD000963.
Torres, O., P. K. Bhartia, J. R. Herman, A. Sinyuk, P. Ginoux, and B. Holben (2001), A long-term record of aerosol optical depth from TOMS observations and comparison to AERONET measurements, *J. Atmos. Sci.*, *59*, 398–413.
Trochkine, D., Y. Iwasaka, A. Matsuki, M. Yamada, Y.-S. Kim, T. Nagatani, D. Zhang, G.-Y. Shi, and Z. Shen (2003), Mineral aerosol particles collected in Dunhuang, China, and their comparison with chemically modified particles collected over Japan, *J. Geophys. Res.*, *108*(D23), 8642, doi:10.1029/2002JD003268.
van de Hulst, H. C. (1981), *Light Scattering by Small Particles*, 470 pp., Dover, Mineola, N. Y.
Volz, F. E. (1973), Infrared optical constants of ammonium sulfate, Sahara dust, volcanic pumice and flyash, *Appl. Opt.*, *12*, 564–568.
Weare, B. C., et al. (1995), Evaluation of total cloudiness and its variability in the Atmospheric Model Intercomparison Project, *J. Clim.*, *8*, 2224–2238.
Weaver, C. J., P. Ginoux, N. C. Hsu, M.-D. Chou, and J. Joiner (2002), Radiative forcing of Saharan dust: GOCART model simulations compared with ERBE data, *J. Atmos. Sci.*, *59*, 736–747.

Werner, M., I. Tegen, S. P. Harrison, K. E. Kohfeld, I. C. Prentice, Y. Balkanski, H. Rodhe, and C. Roelandt (2002), Seasonal and interannual variability of the mineral dust cycle under present and glacial climate conditions, *J. Geophys. Res.*, *107*(D24), 4744, doi:10.1029/2002JD002365.

Woodward, S. (2001), Modeling the atmospheric life cycle and radiative impact of mineral dust in the Hadley Center climate model, *J. Geophys. Res.*, *106*, 18,155–18,166.

Yung, Y. L., T. Lee, C.-H. Wang, and Y.-T. Shieh (1996), Dust: A diagnostic of the hydrologic cycle during the last glacial maximum, *Science*, *271*, 962–963.

Zender, C. S., H. Bian, and D. Newman (2003a), Mineral Dust Entrainment and Deposition (DEAD) model: Description and 1990s dust climatology, *J. Geophys. Res.*, *108*(D14), 4416, doi:10.1029/2002JD002775.

Zender, C. S., D. Newman, and O. Torres (2003b), Spatial heterogeneity in aeolian erodibility: Uniform, topographic, geomorphic, and hydrologic hypotheses, *J. Geophys. Res.*, *108*(D17), 4543, doi:10.1029/2002JD003039.

R. L. Miller, Department of Applied Physics, Armstrong 550, Columbia University, New York, NY 10025, USA. (rlm15@columbia.edu)

J. Perlwitz, Department of Applied Physics, Armstrong 670, Columbia University, New York, NY 10025, USA. (jperlwitz@giss.nasa.gov)

I. Tegen, Max Planck Institut für Biogeochemie, 07701 Jena, Germany. (itegen@bgc-jena.mpg.de)